Pure Appl. Geophys. 183 (2026), 363–387

https://doi.org/10.1007/s00024-025-03883-z

Pure and Applied Geophysics

The Role of the Background Velocity Model for the Marchenko Focusing of Reflected and Refracted Waves

Mert Sinan Recep Kiraz,[1] Roel Snieder,[1] and Kees Wapenaar[2]

Abstract—Marchenko algorithms retrieve the wavefields excited by virtual sources in the subsurface, these are the Green's functions consisting of the primary and multiple reflected waves. The requirements for these algorithms are the same as for conventional imaging algorithms; they need an estimate of the velocity model and the recorded reflected waves. We investigate the dependence of the retrieved Green's functions using the Marchenko equation on the background velocity model and address the question: "How well do we need to know the velocity model for accurate Marchenko focusing?". We present different background velocity models and compare the Green's functions retrieved using these models. We show that these retrieved Green's functions using the Marchenko equation match the exact Green's function with a high accuracy. We also examine the presence of refracted waves in the retrieved Green's function. Marchenko focusing algorithm produces refracted waves only if the initial velocity model used for the iterative scheme is sufficiently detailed to model the refracted waves. We show with numerical examples that the average slowness between the surface and the depth of the focal point is required for an accurate reflected wave retrieval. However, substantially more accurate velocity model knowledge is required in the presence of refracted waves.

Keywords: Computational seismology, seismic interferometry, wave propagation.

1. Introduction

The inverse scattering community utilized the Marchenko equation to relate scattered data to the scattering potential to determine the medium properties (Marchenko, 1955; Gel'fand and Levitan, 1955; Agranovich and Marchenko, 1963; Newton, 1980; Burridge, 1980; Chadan and Sabatier, 1989; Gladwell, 1993; Colton and Kress, 1998). The connection between wavefield focusing and the Marchenko equation was made by Rose (2001, 2002) so that the wavefield focusing at a location in an unknown medium can be achieved once the Marchenko equation is solved. Broggini and Snieder (2012) connect the Marchenko equation and seismic interferometry (Weaver and Lobkis, 2001; Derode et al., 2003; Wapenaar et al., 2005; Snieder and Larose, 2013) and show that one can retrieve the Green's function between any point in the subsurface and points on the acquisition surface without a physical receiver at the virtual source location and with one-sided illumination. Wapenaar et al. (2013) discuss the theory of three-dimensional Green's function retrieval, and present an example of the two-dimensional Green's function retrieval.

A thorough description of the Marchenko redatuming and imaging method and its numerical implementation is given by Wapenaar et al. (2014b), van der Neut et al. (2015), Thorbecke et al. (2017), and Lomas and Curtis (2019). Marchenko methods have been widely used for various applications such as internal multiple elimination (Meles et al., 2015, 2016; Thorbecke et al., 2021), elastic wave applications (da Costa Filho et al., 2014, 2015; Wapenaar, 2014; Reinicke et al., 2020), subsurface imaging and for comparisons with the conventional imaging results (e.g., reverse time migration) (Behura et al., 2014; Wapenaar et al., 2014b; Ravasi et al., 2016; Jia et al., 2018). Additionally, various field data set applications of the Marchenko method have been performed such as imaging of a North Sea field data set (Ravasi et al., 2016), target-oriented subsalt

[1] ExxonMobil Technology and Engineering Company, Spring, TX 77389, USA. E-mail: mertkiraz@gmail.com; roelsnieder@outlook.com

[2] Department of Geoscience and Engineering, Delft University of Technology, P.O. Box 5048, Delft GA 2600, The Netherlands. E-mail: c.p.a.wapenaar@tudelft.nl

imaging of the Gulf of Mexico data set (Jia et al., 2018), time-lapse monitoring of the Frio carbon sequestration data set (Kiraz and Nowack, 2018), multiple suppression on an Arabian Gulf field data set (Staring et al., 2021), and an offshore Brazil data set for imaging a reservoir under basalt (Jia et al., 2021). With growing interest in machine learning applications in seismology, a convolutional neural network-based 1D wavefield focusing is proposed by Kiraz and Snieder (2022).

Recent studies have aimed to address the limitations of the up/down separation of the Marchenko equation. Using the data collected on a closed received array, Kiraz et al. (2020, 2021) retrieve the full-field (e.g., without component separation) Green's function, and show that the full-field Marchenko focusing provides better focusing results in the subsurface than achievable using only the direct waves of the transmission Green's function to the focal point. Diekmann and Vasconcelos (2021)

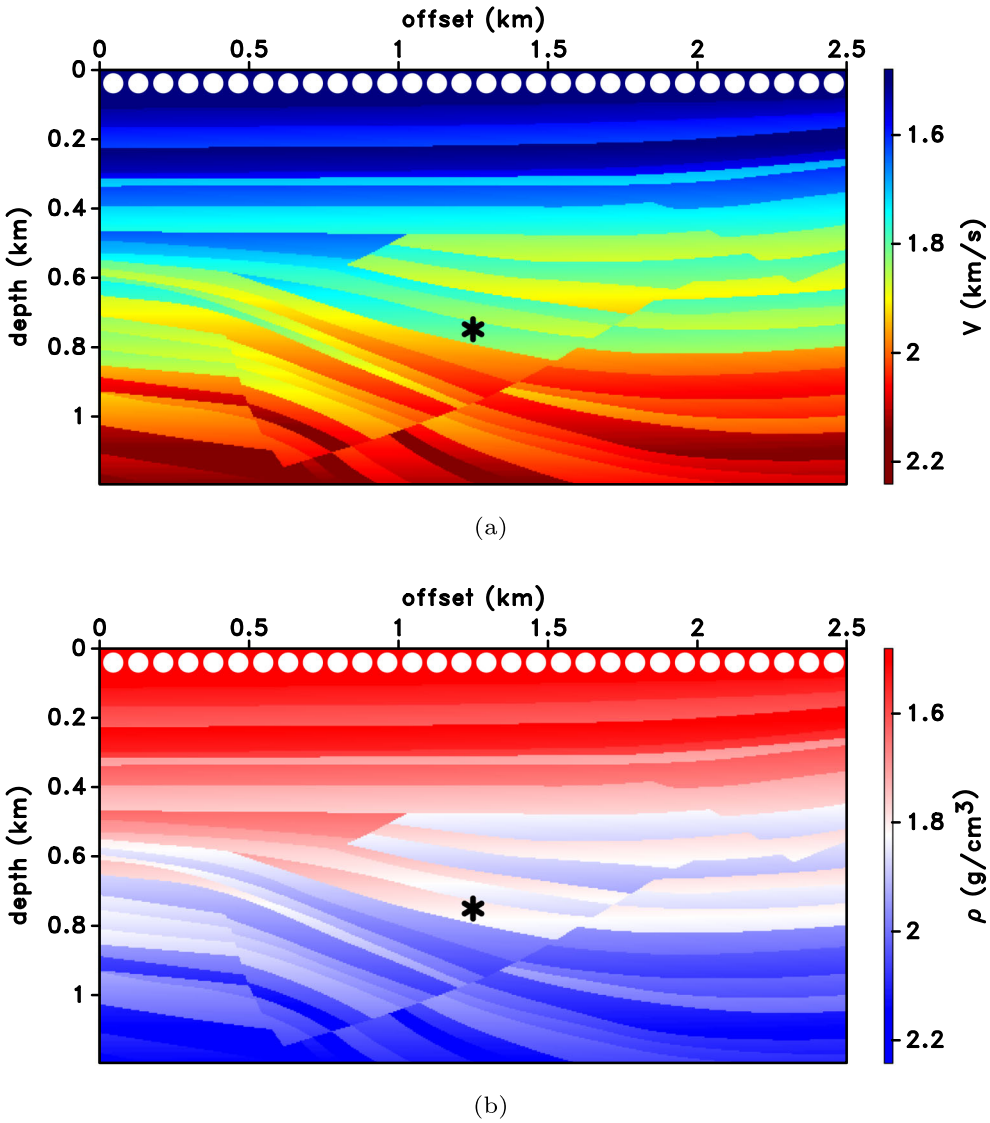

Figure 1
a Velocity model and **b** density model of the synthetic example which are extracted from the Sigsbee model. The black asterisk shows the virtual source location and the white dots at the top indicate every 30th source/receiver location

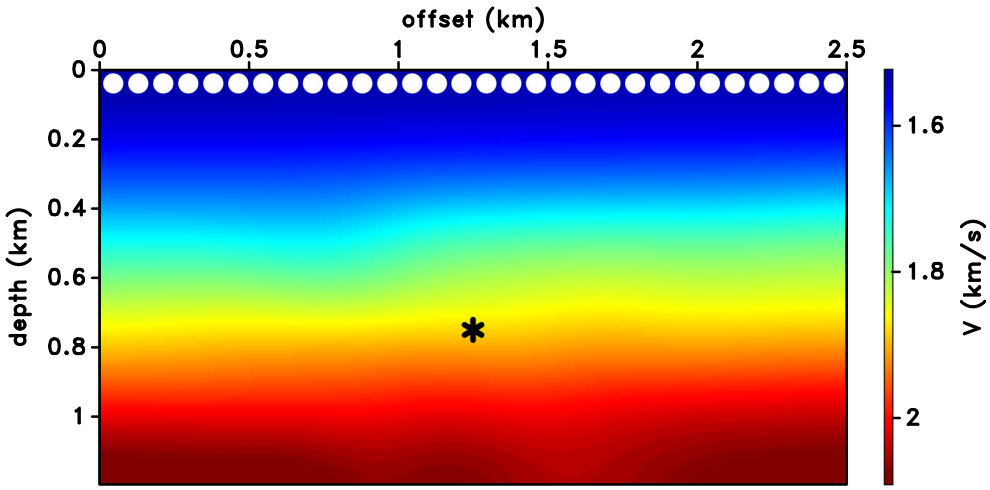

Figure 2
Smoothed version of the velocity model used for the iterative algorithm. The black asterisk shows the virtual source location and the white dots at the top indicate every 30th source/receiver location

and Wapenaar et al. (2021) show alternative methods where one can retrieve the Green's function using single-sided acquisition data without up/down decomposition.

We illustrate the velocity model dependence of the Marchenko method for the reflected and refracted waves only using numerical examples. Providing a theoretical link between the Marchenko algorithm's accuracy as a function of the velocity model as well as an application in imaging using the Marchenko redatumed Green's functions are beyond the scope of this paper. In this paper, we use the one-sided Marchenko focusing to retrieve the Green's function at an arbitrary depth location using different subsurface models with variable velocity and variable density profiles. In Sect. 2, we describe the Marchenko focusing algorithm and show that it requires only two inputs; surface-recorded data and the initial estimate of the velocity model, which are the same inputs as for conventional imaging algorithms. In Sect. 3, we provide a visual tour to describe the iterative Marchenko focusing algorithm. In Sect. 4, we assess the background velocity model dependence of the Marchenko method and assess the accuracy of the retrieved Green's function by presenting correlation coefficients (CCs) between the retrieved and numerically modeled Green's functions. Lastly, in Sect. 5, we use the Marmousi model to investigate the presence of the refracted waves in the Marchenko focusing, and show that the presence of the refracted waves depends only on the initial estimate of the velocity model.

2. Methodology

We use the Marchenko algorithm proposed by Wapenaar et al. (2013) which builds on earlier work of Rose (2001), Rose (2002), and Broggini and Snieder (2012). We denote spatial coordinates as $\mathbf{x} = (x, z)$, and the receiver coordinates as $\mathbf{x}_R = (x_R, z_R)$. The receivers are located at the transparent acquisition surface at $z = 0$, and the multiples caused by free surface (e.g., air-water interface) are excluded.

We relate the ingoing wave at $z = 0$, U_k^{in}, to the outgoing wave, U_k^{out}, at iteration k as

$$U_k^{out}(\mathbf{x}_R, t) = \int R(\mathbf{x}_R, \mathbf{x}, t) * U_k^{in}(\mathbf{x}, t) dx \,, \qquad (1)$$

where R corresponds to the reflection response of the medium and the asterisk denotes temporal convolution. The iterative scheme starts with modeling the direct wave, and we denote the arrival time of the direct wave from the virtual source location inside the medium, $\mathbf{x}_s$, for which we aim to retrieve the Green's

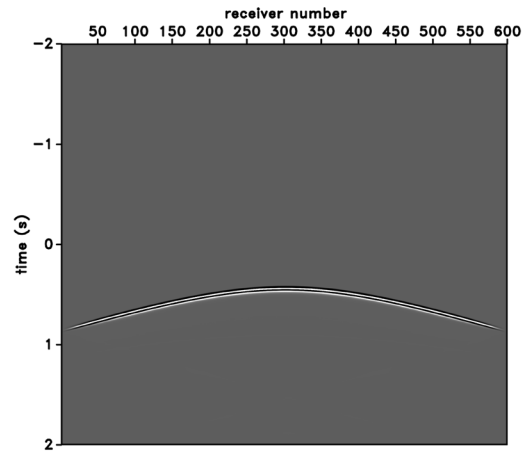
receiver number
50 100 150 200 250 300 350 400 450 500 550 600
time (s)
−2 −1 0 1 2

(a)

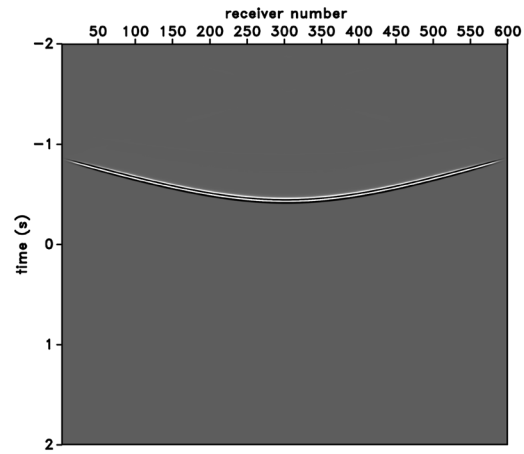
receiver number
50 100 150 200 250 300 350 400 450 500 550 600
time (s)
−2 −1 0 1 2

(b)

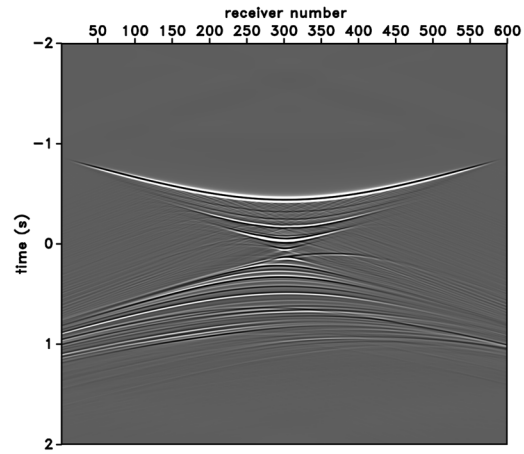
receiver number
50 100 150 200 250 300 350 400 450 500 550 600
time (s)
−2 −1 0 1 2

(c)

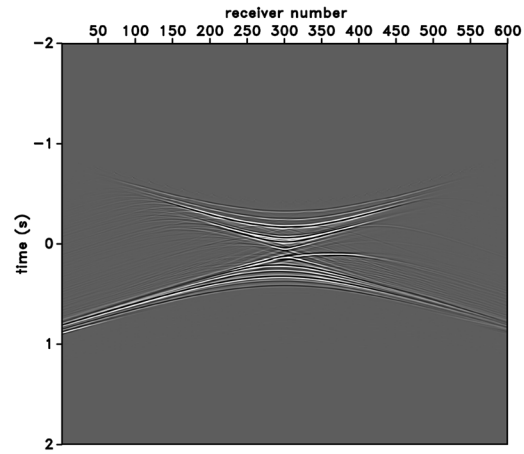
receiver number
50 100 150 200 250 300 350 400 450 500 550 600
time (s)
−2 −1 0 1 2

(d)

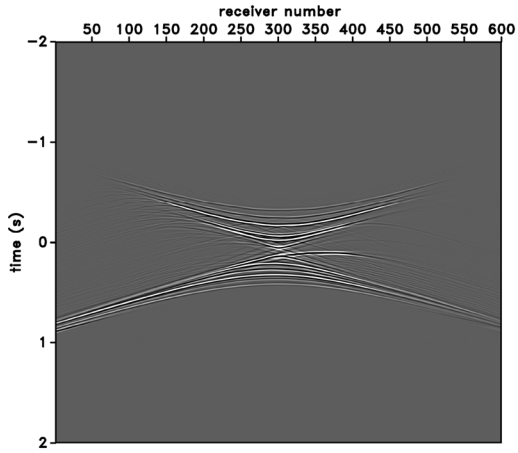
receiver number
50 100 150 200 250 300 350 400 450 500 550 600
time (s)
−2 −1 0 1 2

(e)

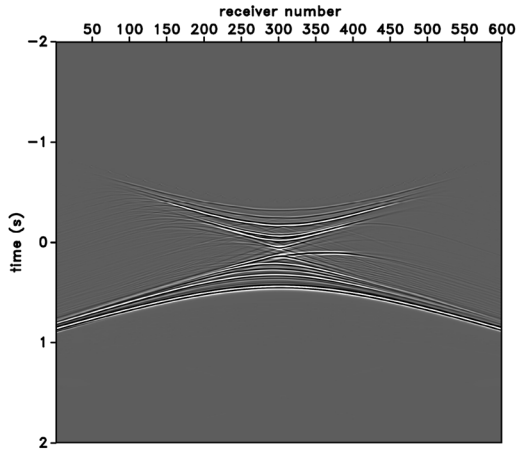
receiver number
50 100 150 200 250 300 350 400 450 500 550 600
time (s)
−2 −1 0 1 2

(f)

◀Figure 3
a Modeled direct wave. **b** Time-reversed direct wave. **c** Recorded wavefield for the first iteration after sending in the time-reversed direct wave. **d** Wavefield after windowing applied. **e** Wavefield after multiplying with (-1). **f** Wavefield after adding the modeled direct wave. This is also the input for the second iteration

function, to the receivers at the surface as t_d. Following Broggini and Snieder (2012), we design an iterative scheme so that at $t = 0$, the wavefield becomes a delta function at the pre-defined focal (or virtual source) location. We start the iterative algo-

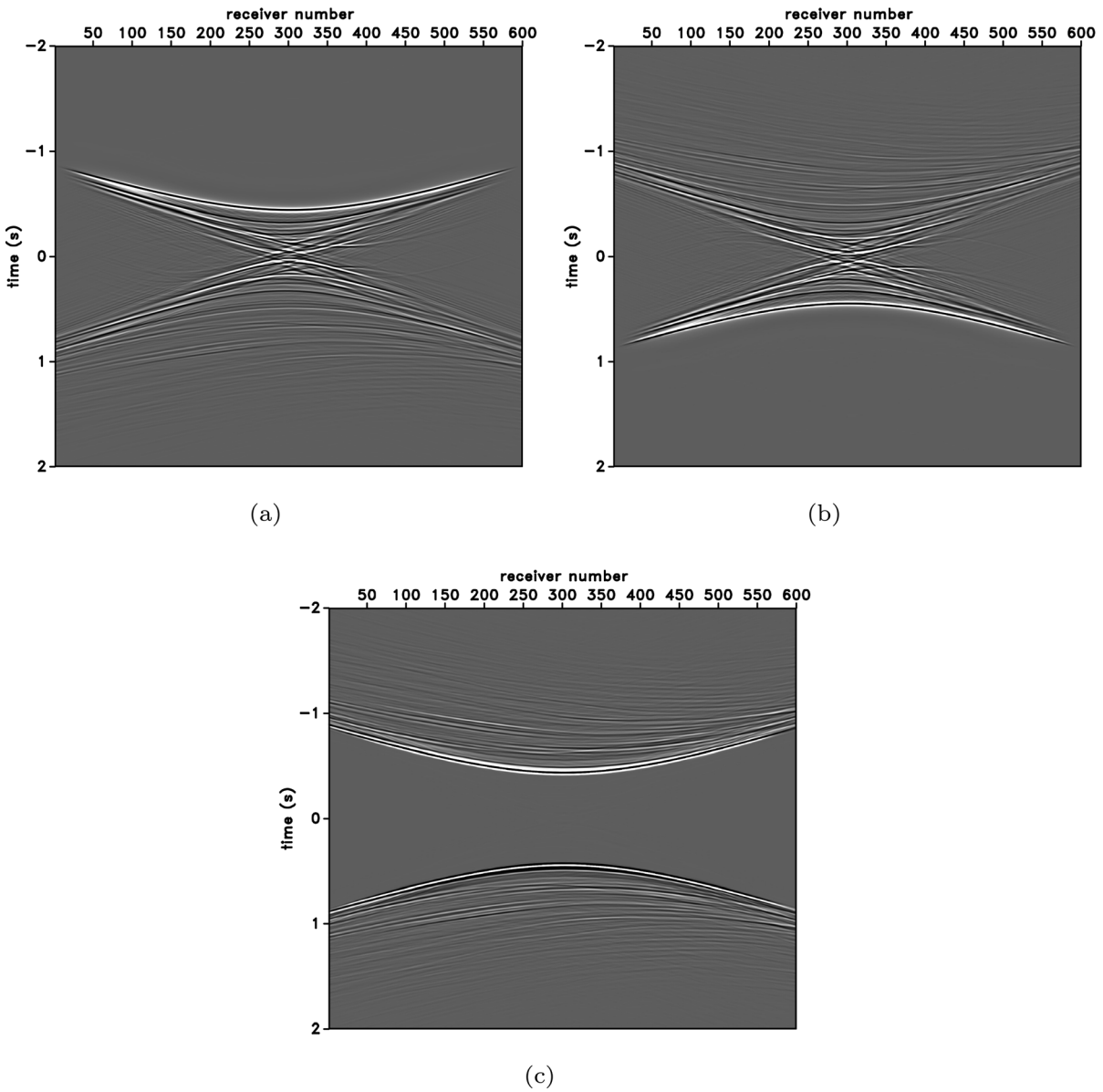

Figure 4
a $U_{total}(\mathbf{x}, t)$ for the fourth iteration. **b** $U_{total}(\mathbf{x}, -t)$ for the fourth iteration. **c** $G_h(\mathbf{x}, \mathbf{x}_s, t) = U_{total}(\mathbf{x}, t) - U_{total}(\mathbf{x}, -t)$ for the fourth iteration

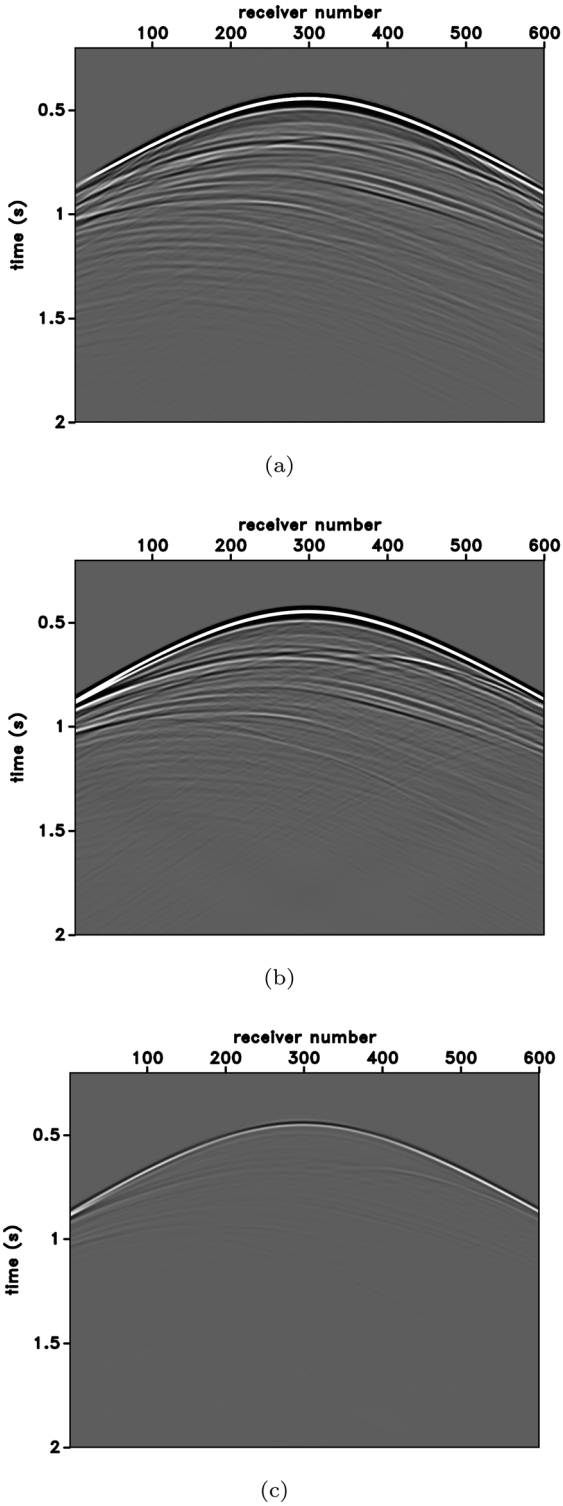

◀Figure 5
a Retrieved Green's function using the Marchenko focusing (times when $t > 0$ of G_h in Fig. 4c). **b** Numerically modeled Green's function. **c** Difference between the numerically modeled Green's function in **a** and the retrieved Green's function in **b**

rithm by defining the ingoing wavefield at $z = 0$ for iteration k as

$$U_k^{in}(\mathbf{x},t) = U_0^{in}(\mathbf{x},t) - \Theta(\mathbf{x},t)U_{k-1}^{out}(\mathbf{x},-t)\ , \qquad (2)$$

where $\Theta(\mathbf{x},t)$ defines a window function and U_0^{in} is the time-reversed direct wave between $\mathbf{x}_s$ inside the medium and $\mathbf{x}$ at the surface. We define the window function such that $\Theta(\mathbf{x},t) = 1$ when $-t_d^{\epsilon}(\mathbf{x}) < t < t_d^{\epsilon}(\mathbf{x})$ and otherwise $\Theta(\mathbf{x},t) = 0$ with $t_d^{\epsilon} = t_d - \epsilon$. We introduce ϵ as a small positive constant to exclude the direct wave at t_d. After the convergence is achieved (i.e., $U_k^{out} = U_{k-1}^{out}$) we can drop the iteration number, and insert equation (2) into equation (1), and obtain

$$\begin{aligned} U^{out}(\mathbf{x}_R,t) = &\int R(\mathbf{x}_R,\mathbf{x},t) * U_0^{in}(\mathbf{x},t)\ dx \\ &- \int R(\mathbf{x}_R,\mathbf{x},t) * \Theta(\mathbf{x},t)U^{out}(\mathbf{x},-t)\ dx\ . \end{aligned} \qquad (3)$$

Once the convergence is achieved, we denote the recorded data at the receivers as $U_{total}(\mathbf{x},t) = U^{in}(\mathbf{x},t) + U^{out}(\mathbf{x},t)$ which consists of the superposition of the ingoing and outgoing wavefield. We obtain the homogeneous Green's function ($G_h(\mathbf{x},\mathbf{x}_s,t) = G(\mathbf{x},\mathbf{x}_s,t) - G(\mathbf{x},\mathbf{x}_s,-t)$) (Oristaglio, 1989), for the virtual source location $\mathbf{x}_s$ and the receiver location $\mathbf{x}$ as

$$G_h(\mathbf{x},\mathbf{x}_s,t) = U_{total}(\mathbf{x},t) - U_{total}(\mathbf{x},-t)\ . \qquad (4)$$

Equation (4) satisfies the homogeneous wave equation and, hence, retrieves the Green's function for times $t > 0$ for the virtual source location $\mathbf{x}_s$ (Oristaglio, 1989; Wapenaar et al., 2013; Kiraz et al., 2021). The iterative scheme we use follows the algorithm presented by Wapenaar et al. (2013), and equations (1), (2), and (4) are given in Wapenaar et al. (2013) in equations (13), (12), and (14), respectively.

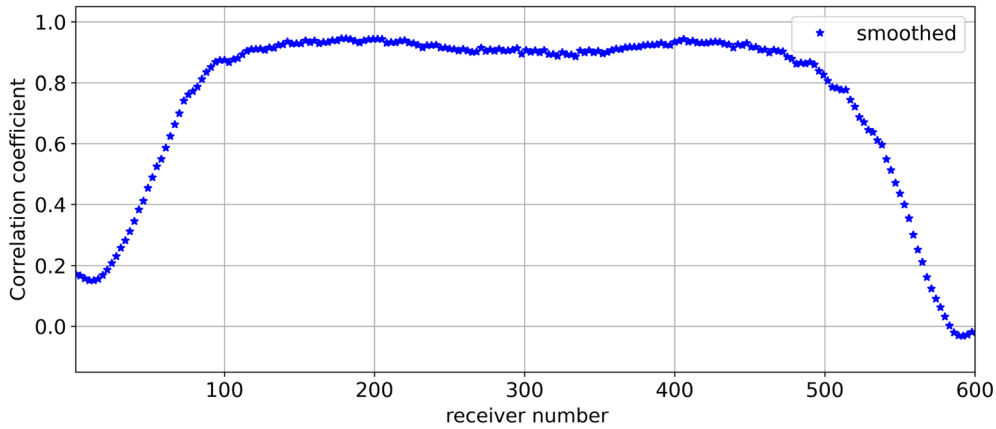

Figure 6
Trace-by-trace calculated correlation coefficient between the retrieved Green's function (Fig. 5a) and the numerically modeled Green's function (Fig. 5b)

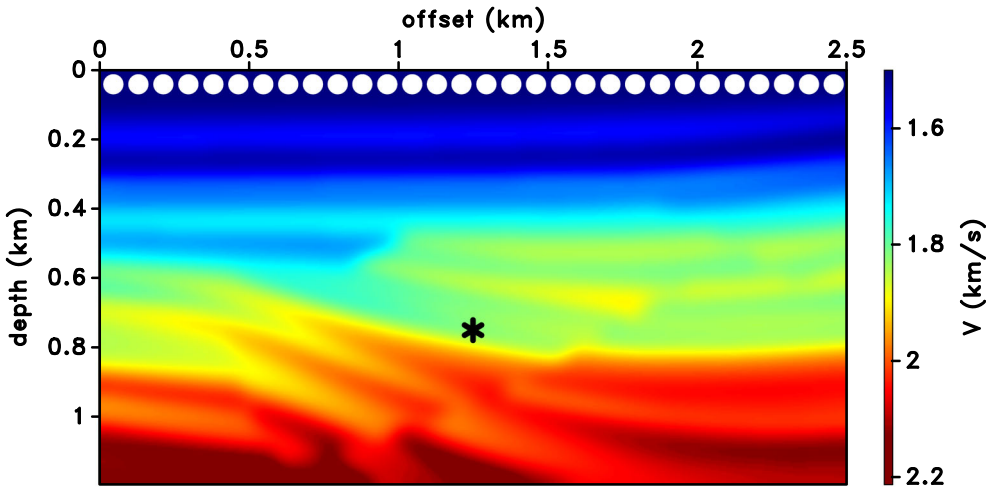

Figure 7
Less smoothed version of the velocity model used for the iterative algorithm. The black asterisk shows the virtual source location and the white dots at the top indicate every 30th source/receiver location

3. *Visualizing the Iterative Scheme*

In this section, we present a numerical example to aid the visual understanding of the iterative scheme described in Sect. 2. Figure 1 shows the subsurface model and source and receiver geometry of our first numerical experiment. Figure 1a and b show the variable velocity and density models used for the numerical example, respectively, which are extracted from the Sigsbee model (Paffenholz et al., 2002) with 2.5 km horizontal and 1.2 km vertical extent. The virtual source location is at x_s = 1.25 km and z_s = 0.75 km in depth which is shown with the black asterisk in Fig. 1. The white dots located at the surface of the models in Fig. 1 represent every 30th receiver location. We use point impulsive sources and record pressure at the receivers, and exclude the presence of free surface. During the iterative Marchenko scheme, we use the normal derivative of the input pressure data to send the wavefield into the medium from the receiver array (Kiraz et al., 2021).

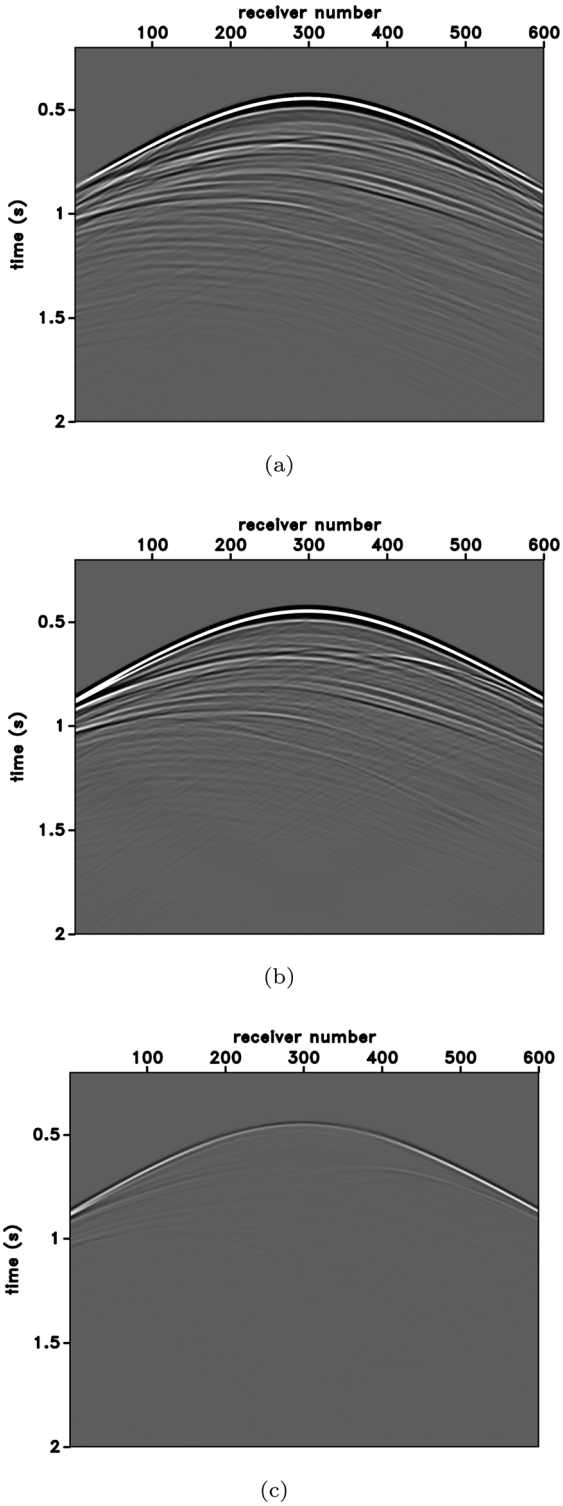

Figure 2 shows the smoothed version of the velocity model which is obtained by smoothing the slowness. This model is so strongly smoothed that it presents mostly one-dimensional information about the velocity. As we follow the iterative scheme described in Sect. 2, the first step is to model the direct wave using the smooth background velocity model (shown in Fig. 2). Figure 3a shows the modeled direct wave. After modeling the direct wave, the next step is to time-reverse the direct wave which is shown in Fig. 3b. We then emit the time-reversed direct wave from the boundary into the medium. However, one can also convolve the time-reversed direct wave with the reflection response when forward modeling in the true medium is not applicable. Figure 3c shows the recorded data at the receiver array after sending in the time-reversed direct wave (Fig. 3b) from the receiver array located at the surface of the medium. We use Fig. 3a and b to define the window function (Θ in Eq. (2)). After applying this window function to the recorded data shown in Fig. 3c, d shows the muted data. Following the iterative algorithm, we next negate the muted data ((−) sign in Eq. (2)) and the resulting wavefield is shown in Fig. 3e. As the last step, we add the direct wave (Fig. 3a) to this wavefield (time reverse of U_0^{in} in Eq. (2)) and Fig. 3f shows the combined wavefield (time reverse of U_k^{in} in Eq. (2)). The time-reverse version of the wavefield shown in Fig. 3f is, therefore, the input for the second iteration and is ready to be emitted back into the medium using the receiver array at the surface.

◀Figure 8
a Retrieved Green's function using the Marchenko focusing using the less smooth velocity model. **b** Numerically modeled Green's function (which is the same wavefield as Fig. 5b). **c** Difference between the numerically modeled Green's function in **a** and the retrieved Green's function in **b**

Figure 4a shows $U_{total}(\mathbf{x}, t)$ obtained after the fourth iteration of the iterative scheme. Note that Fig. 4a is nearly symmetric in time for the times $-t_d < t < t_d$, defined using the arrival time of the direct wave (approximately between -1 s and 1 s). Figure 4b shows $U_{total}(\mathbf{x}, -t)$ for the fourth iteration which is the time-reversed recorded data at the receivers obtained after the fourth iteration. Figure 4c shows the homogeneous Green's function, $G_h(\mathbf{x}, \mathbf{x}_s, t)$ (see Eq. (4)), for the fourth iteration.

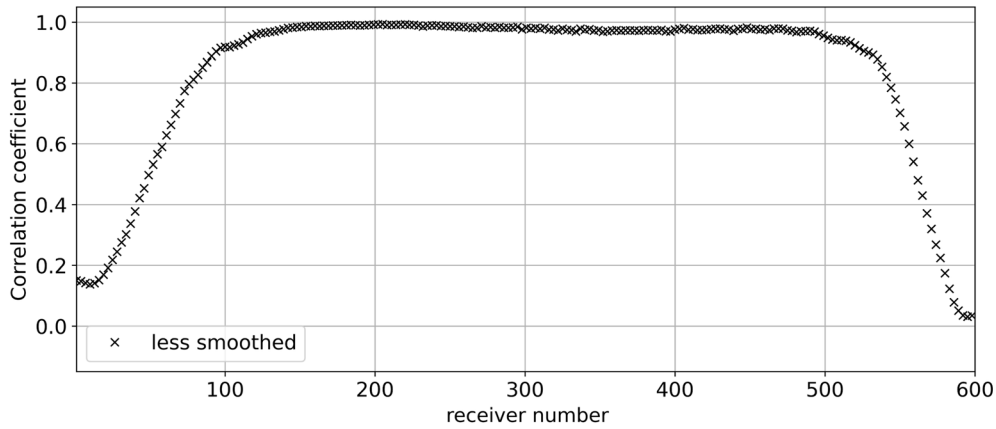

Figure 9
Trace-by-trace calculated correlation coefficient between the retrieved Green's function (Fig. 8a) and the numerically modeled Green's function (Figs. 5b and 8b) for the velocity model of Fig. 7

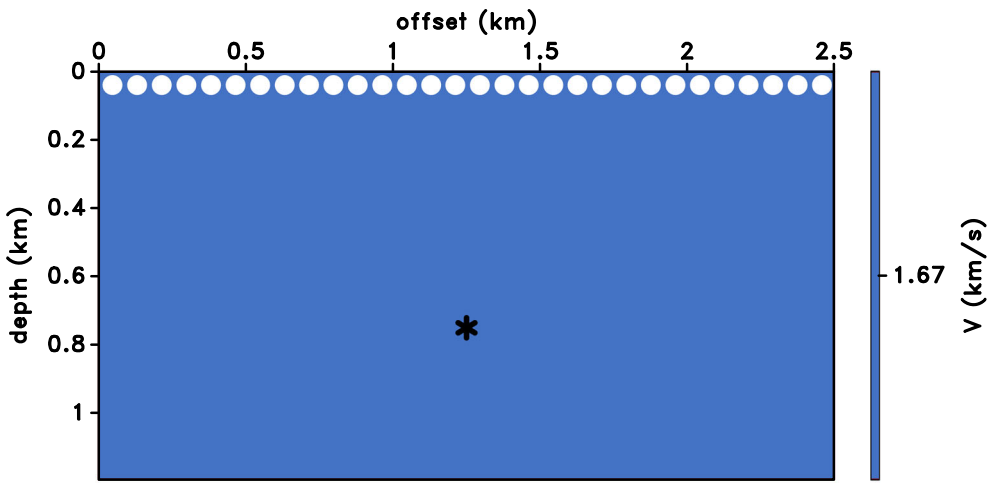

Figure 10
Constant velocity model used for the iterative algorithm. The black asterisk shows the virtual source location and the white dots at the top indicate every 30th source/receiver location

Figure 5a shows $G_h(\mathbf{x}, \mathbf{x}_s, t)$ for the fourth iteration for positive times only which is the retrieved Green's function and Fig. 5b shows the numerically modeled Green's function for the virtual source location. The difference between the numerically modeled and retrieved Green's functions is shown in Fig. 5c. Figure 5 shows that the numerically modeled Green's function closely matches the retrieved Green's function for $t \geq t_d$. However, we also see in Fig. 5c that there are overall mismatches in amplitudes and right and left edges of the wavefield that are due to the limited aperture used during the injection of the wavefield back into the medium from the receiver array.

We quantify the accuracy of the Green's function retrieval using the Marchenko equation results by calculating trace-by-trace CCs between the retrieved Green's function and the numerically modeled Green's function. We use the Pearson correlation coefficient (Rodgers and Nicewander, 1988) as a metric to quantitatively measure the correlations between the retrieved and numerically modeled

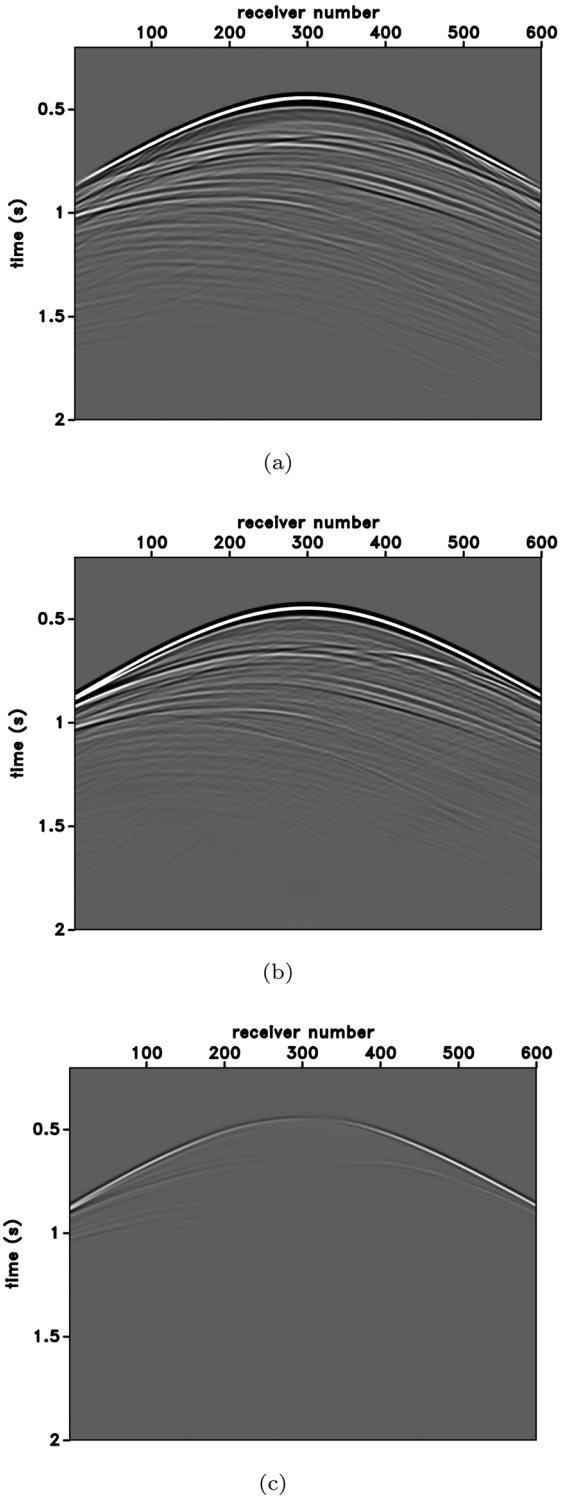

Green's functions. We calculate the trace-by-trace CCs using the full trace including the direct wave.

◀Figure 11
a Retrieved Green's function using the Marchenko focusing using the constant velocity model. **b** Numerically modeled Green's function (which is the same wavefield as Figs. 5b and 8b). **c** Difference between the numerically modeled Green's function in **a** and the retrieved Green's function in **b**

The CCs between the retrieved Green's function (Fig. 5a) using the smoothed version of the velocity model and the numerically modeled Green's function (Fig. 5b) are shown in Fig. 6. The average CC in Fig. 6 is 0.76. The low CCs around the right and left edges of the CC plot in Fig. 6 are due to the limited aperture used during the injection of the wavefield. For the receivers where the limited aperture effects are not evident (receivers from 100 to 500), the average CC is 0.91. This shows a high accuracy Green's function retrieval by the Marchenko focusing algorithm using the smoothed version of the velocity model (Fig. 2).

4. Importance of the Initial Background Velocity Model

In this section, we investigate the effect of the smoothness of the background velocity model on the retrieved Green's function. The second numerical example consists of the same velocity and density models as with the first example (see Fig 1a and b); however, this time we use a more detailed (or less smoothed) version of the background velocity model which is shown in Fig. 7 than the one presented in Fig. 2 to retrieve the Green's function using the Marchenko focusing. As with the iterative algorithm, we use the more detailed velocity model to produce the direct wave and initiate the iterative scheme. By following the steps presented in Fig. 3, we retrieve the Green's function. Figure 8a shows G_h for the fourth iteration for positive times only (being the retrieved Green's function) and Fig. 8b shows the numerically modeled Green's function for the virtual source location. The difference between the numerically modeled Green's function (Fig. 8b) and the retrieved Green's function Fig. 8a is shown in Fig. 8c. Similar to Fig. 5c, Fig. 8c shows that the

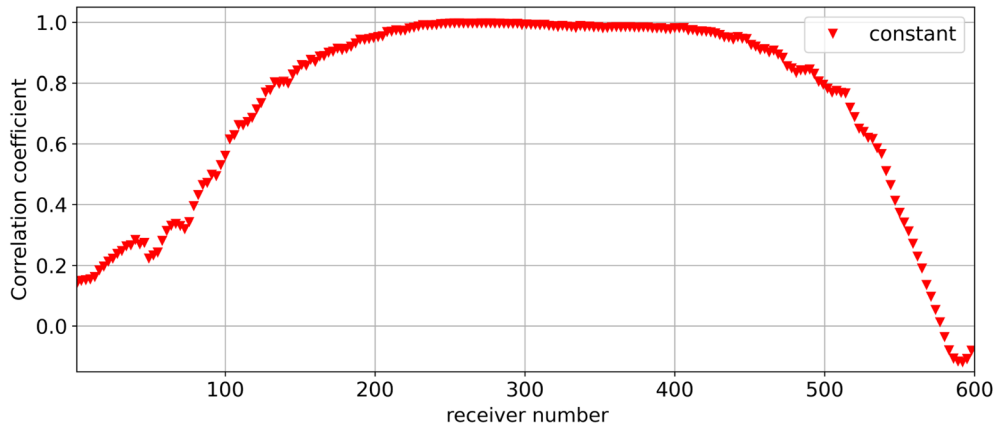

Figure 12
Trace-by-trace calculated correlation coefficient between the retrieved Green's function (Fig. 11a) and the numerically modeled Green's function (Figs. 5b, 8b, and 11b) for the constant velocity model in Fig. 10

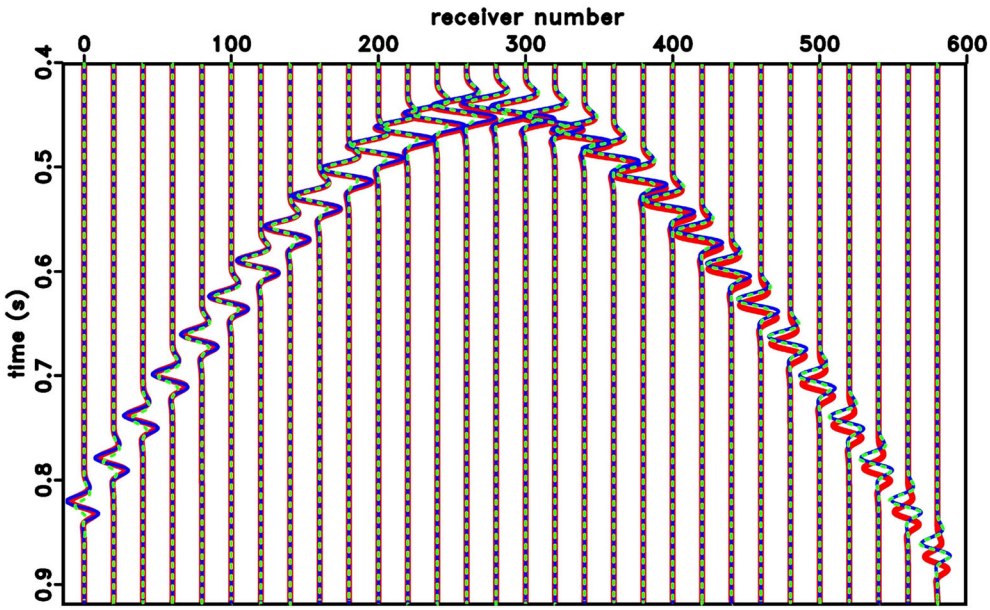

Figure 13
Comparison of the modeled direct waves using the velocity models shown in Figs. 7 (thin blue lines) and 10 (thick red lines), overlain with the direct wave modeled using the true velocity model in Fig. 1a (dashed green lines). The traces have been multiplied by $exp(2t)$

retrieved and modeled Green's functions have mismatches in overall amplitude, and the right and left wavefield edges.

To quantify the quality of the retrieved Green's function using the more detailed velocity model (Fig. 7), we calculate the CCs between the retrieved Green's function (Fig. 8a) and the numerically modeled Green's function (Fig. 8b), which are shown in Fig. 9. The average CC in Fig. 9 is 0.83, and the average CC for receivers from 100 to 500 is 0.98. Therefore, by using a more detailed version of the velocity model (Fig. 7) for the iterative scheme, we retrieve the Green's function by the Marchenko focusing algorithm with a higher CC than the one presented in Fig. 6.

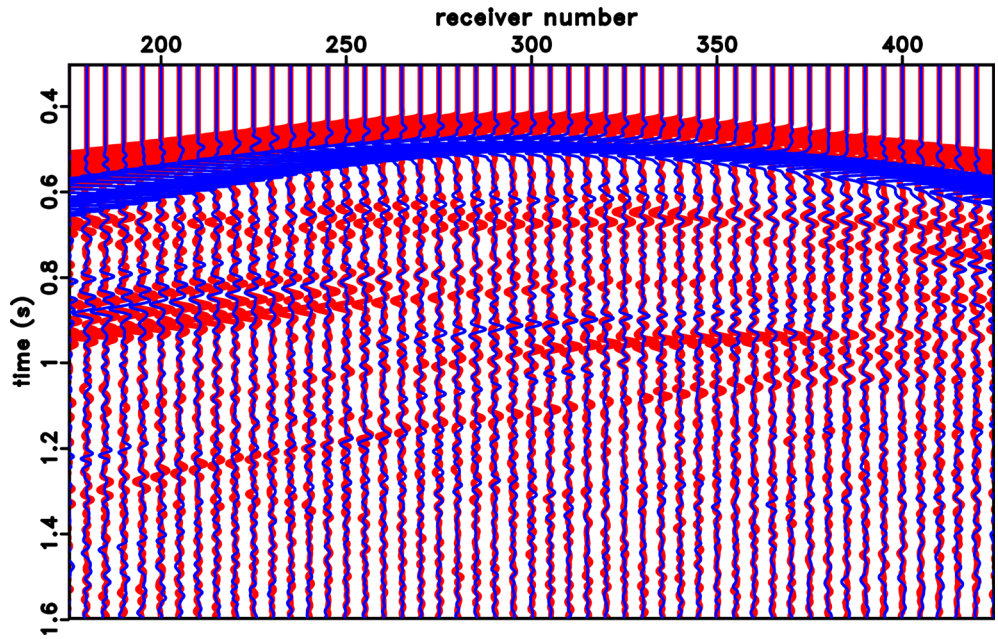

Figure 14
The retrieved Green's function using the constant background velocity model with 10% error (blue lines) and the modeled Green's function (red lines). The traces have been multiplied by $exp(2t)$ to emphasize the match for the later times

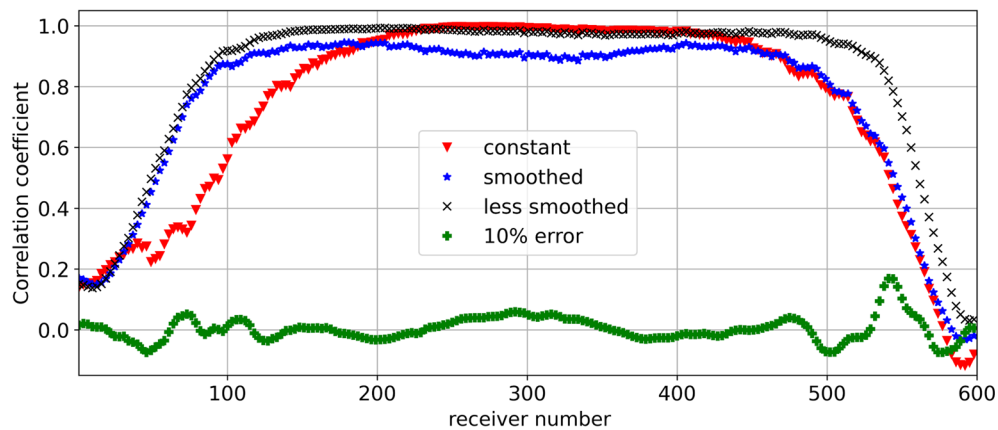

Figure 15
Trace-by-trace calculated between the numerically modeled Green's function (Figs. 5b, 8b, and 11b) and the retrieved Green's functions using the velocity models from Figs. 2, 7, 10, and the velocity model in Fig. 10 with 10% error

As the last step of the velocity model sensitivity analysis, we use a constant velocity model. As opposed to the first two velocity models used (see Figs. 2 and 7), the constant velocity model does not include any geological or geophysical information, including about the possible dipping layers and the velocity variations. The constant value of the velocity is calculated using the average slowness between the surface and the depth of the focal point and is shown in Fig. 10, which is used to model the direct wave for the iterative algorithm. After following the iterative scheme, Fig. 11a shows G_h for the fourth iteration for positive times only (the retrieved Green's function), and Fig. 11b shows the numerically modeled Green's

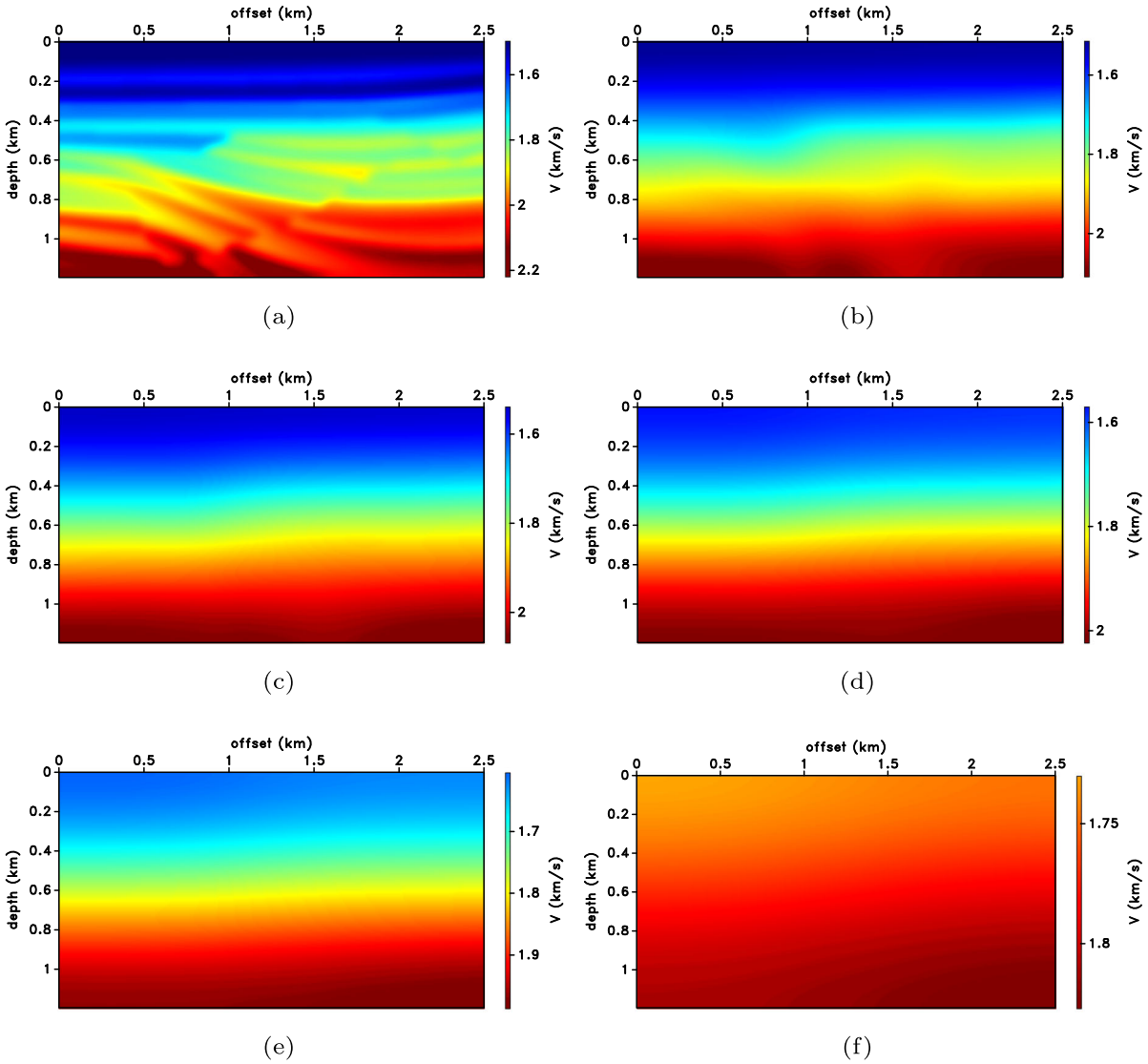

Figure 16
Velocity model in Fig. 1a after applying smoothing with a radius of 0.05 km, 0.25 km, 0.45 km, 0.65 km, 0.85 km, and 1.2 km, shown in **a**, **b**, **c**, **d**, **e**, and **f**, respectively

function for the virtual source location. Figure 11c shows the difference between the numerically modeled Green's function (Fig. 11b) and the retrieved Green's function (Fig. 11a). The difference between the numerically modeled and the retrieved Green's functions in Fig. 11c using the constant velocity model (Fig. 10) is similar to the ones presented in Figs. 5c and 8c. There are also mismatches in overall amplitudes at the right and left wavefield edges.

Similar to the previous examples, we show the accuracy of the retrieved Green's function using the constant velocity model (Fig. 10) by calculating the CCs between the retrieved (Fig. 11a) and the numerically modeled (Fig. 11b) Green's functions, which are shown in Fig. 12. The average CC in Fig. 12 is 0.73; however, the average CC for receivers from 100 to 500 is 0.93. The CC for receivers from 100 to 500 in Fig. 12 is higher than the one presented in Fig. 6 for receivers from 100 to 500;

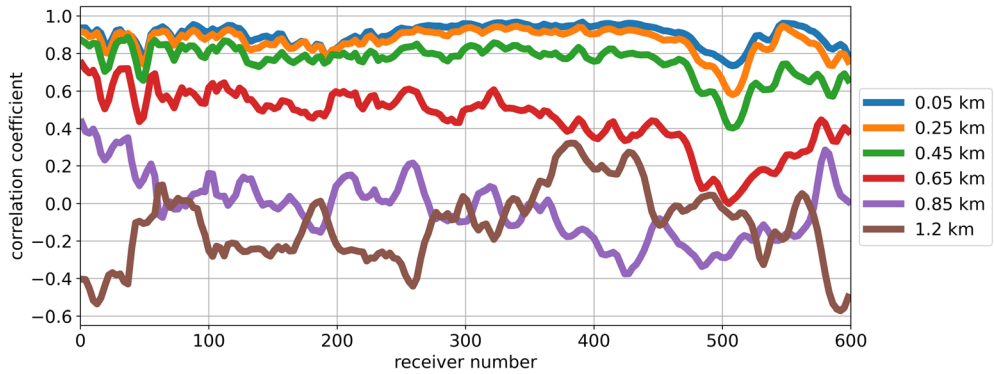

Figure 17
CCs between the numerically modeled and retrieved Green's functions using the smoothing radius of 0.05 km, 0.25 km, 0.45 km, 0.65 km, 0.85 km, and 1.2 km, denoted with the blue, orange, green, red, purple, and brown lines, respectively

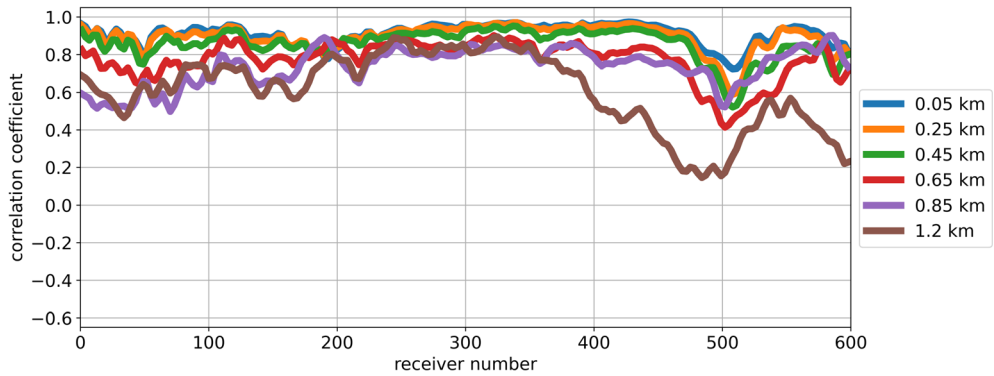

Figure 18
CCs after applying a time shift of 0.8 ms, 1.2 ms, 2.4 ms, 4.8 ms, 9.6 ms, and 25.6 ms to the retrieved Green's functions using the velocity models shown in Fig. 16 using the smoothing radius of 0.05 km, 0.25 km, 0.45 km, 0.65 km, 0.85 km, and 1.2 km, respectively

however, the CC for receivers from 0 to 600 in Fig. 12 is lower than the CC presented in Fig. 6. Using a constant velocity model for the iterative scheme, we retrieve just as accurate Green's function for one virtual source location as with using the smoothed velocity model for the Marchenko focusing algorithm.

As described and shown in Sects. 2 and 3, we model the direct wave using the background velocity model and start the iterative scheme. To evaluate the differences only in the modeled direct waves using different velocity models (Figs. 7, 10), we show in Fig. 13 the comparison of the modeled direct waves using the velocity models shown in Figs. 7 (thin blue lines) and 10 (thick red lines), overlain with the direct wave modeled using the true velocity model in Fig. 1a (dashed green lines). For the receivers between 100 and 500 in Fig. 13, the modeled direct waves are almost identical for the less smoothed velocity model (thin blue lines) and constant velocity model (thick red line) with the true velocity model (dashed green line). This high similarity in the modeled direct waves also produces the high-accuracy CCs (Figs. 9, 12).

We further test the sensitivity of the Marchenko method to the velocity model by adding a 10% error to the velocity model shown in Fig. 10 (which is 1.67 km/s) and assume the constant velocity as 1.5 km/s. We show the retrieved Green's function using the constant background velocity model with 10% error (thin blue lines) and the modeled Green's function (thick red lines) superimposed in Fig. 14 after

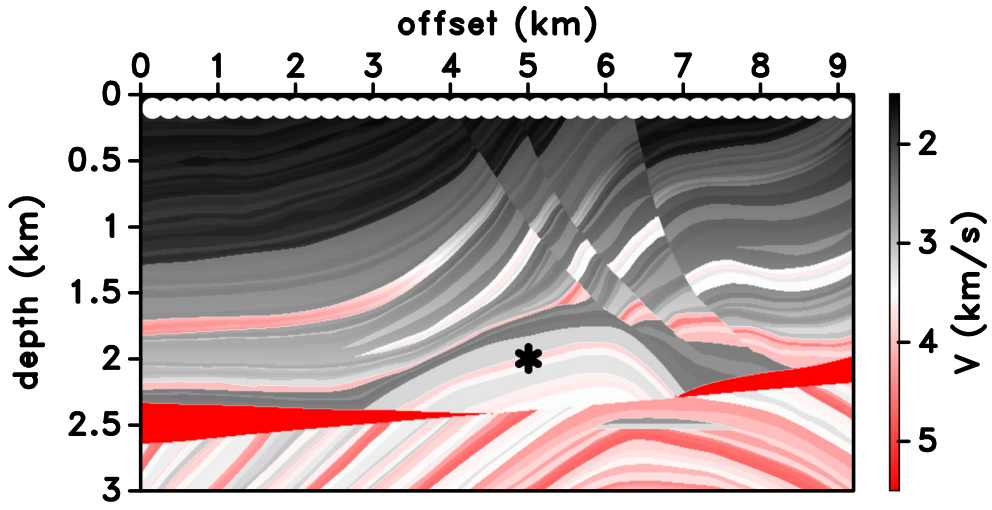

(a)

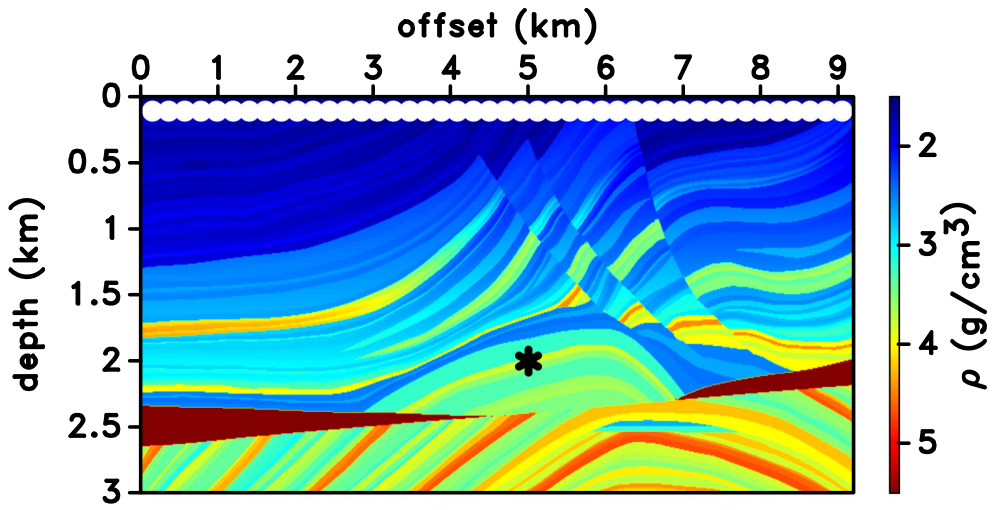

(b)

Figure 19
a Marmousi velocity model and **b** density model of the synthetic example. The black asterisk shows the virtual source location and the white dots at the top indicate every 30th source/receiver location

multiplying traces by $exp(2t)$. The mismatch in time, amplitudes, and phase in Fig. 14 indicate that the constant value of the velocity should be calculated using the average slowness between the surface and the depth of the focal point, and erroneous constant velocity models will not retrieve the accurate Green's function.

We present the CCs in Fig. 15 between the numerically modeled Green's function and the retrieved Green's functions using the velocity models from Figs. 2, 7, 10, and the velocity model in Fig. 10 with 10% error using the blue star markers, the grey cross markers, the red triangle markers, and the green plus markers, respectively. We see in Fig. 15 that the similarity in the modeled direct wave for the Marchenko focusing creates a high accuracy in the retrieved Green's functions. The star, the cross, and the triangle markers show CCs around 0.9; however,

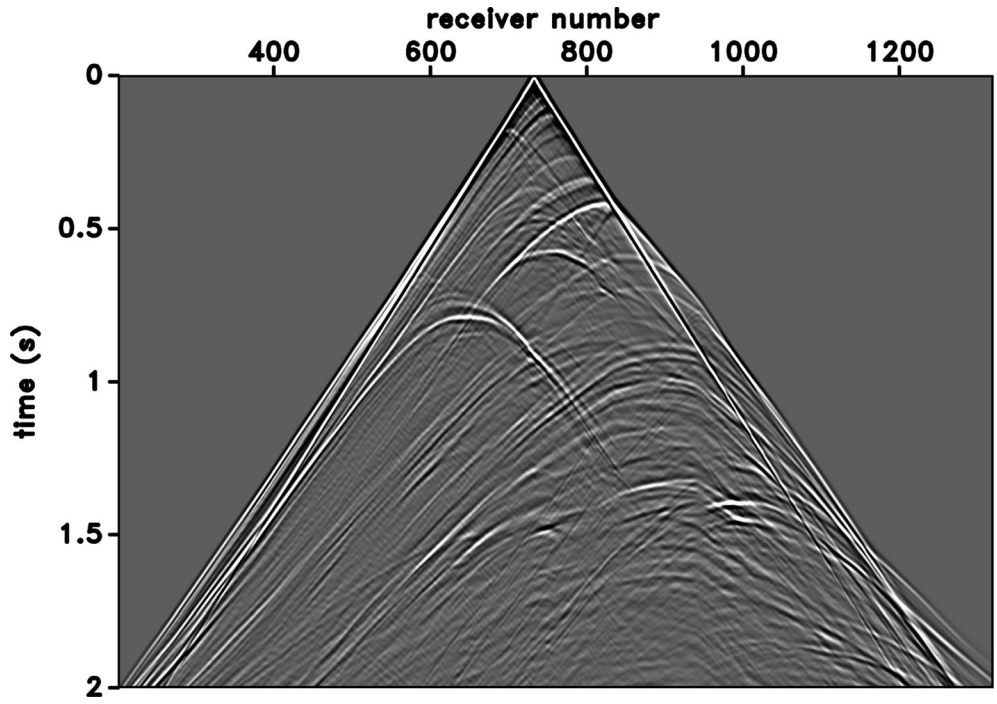

Figure 20
Modeled data using the velocity and density models shown in Fig. 19 with the receivers and source located at the surface

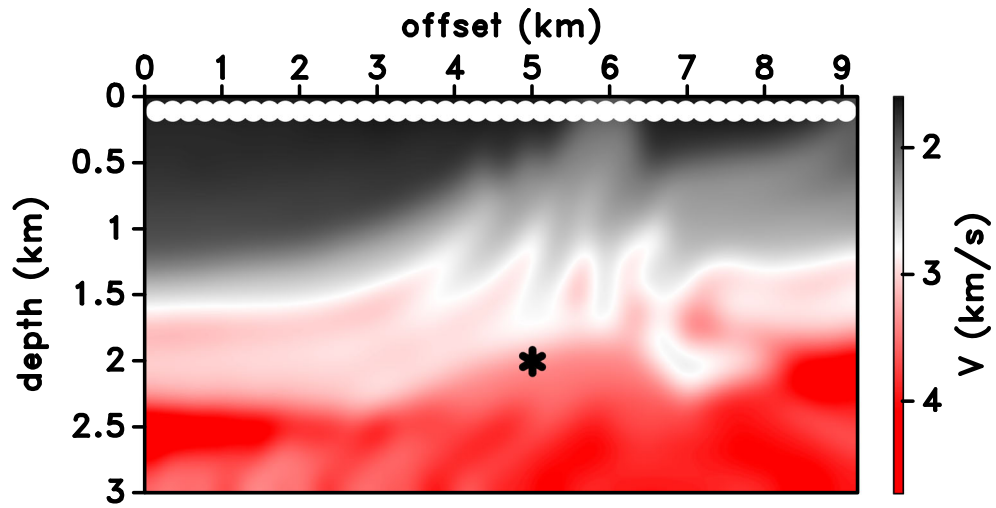

Figure 21
Smoothed version of the Marmousi velocity model used for the iterative algorithm. The black asterisk shows the virtual source location and the white dots at the top indicate every 30th source/receiver location

the green plus marker shows a CC around 0. Therefore, we conclude that the Green's function retrieval using the Marchenko equation successfully retrieves the Green's functions as long as the correct average slowness between the surface and the depth of the focal point is known. For different virtual source

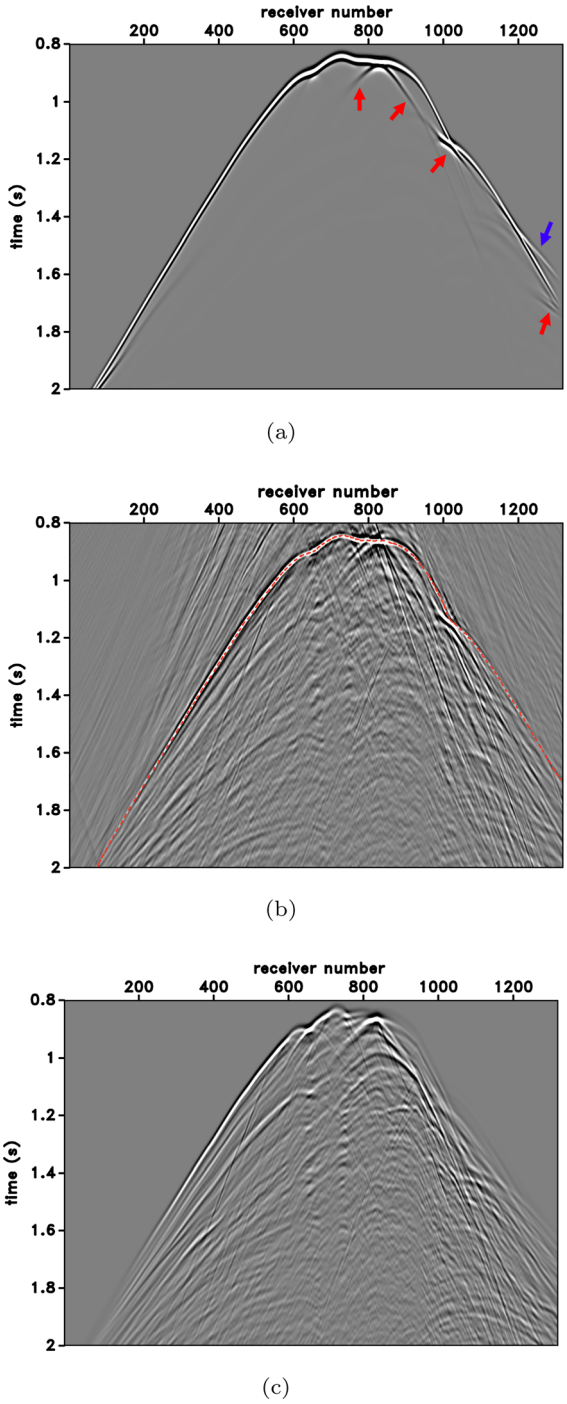

◀Figure 22
a Modeled direct wave using the smoothed version of the Marmousi velocity model given in Fig. 21. The red arrows show some of the triplicated arrivals and the blue arrow shows the refracted wave. **b** Retrieved Green's function using the Marchenko focusing using the smoothed version of the Marmousi velocity model. The red dashed curve shows the arrival of the direct wave (including some triplicated waves), approximately. **c** Numerically modeled Green's function

locations, one needs to have the average slowness between the surface and the depth of the focal point for every virtual source location.

To further investigate the velocity model dependence of the Marchenko algorithm for the reflected wave retrieval, we apply different degrees of smoothing to the velocity model shown in Fig. 1a and calculate the trace-by-trace CCs between the numerically modeled and the retrieved Green's functions. This time we exclude the direct wave so that the CCs quantify the retrieval of the internal multiple reflections. Figure 16a–f show velocity models with a smoothing radius of 0.05 km, 0.25 km, 0.45 km, 0.65 km, 0.85 km, and 1.2 km, respectively, applied on offset and depth (or x and z, respectively) axes using the triangle smoothing filtering in the Madagascar software package (Fomel et al., 2013; Claerbout, 2014). Figure 17 shows the CCs between the numerically modeled and the retrieved Green's functions using the smoothed velocity models shown in Fig. 16. The blue, orange, green, red, purple, and brown lines in Fig. 17 denote the CCs between the numerically modeled and retrieved Green's function using the smoothing radius of 0.05 km, 0.25 km, 0.45 km, 0.65 km, 0.85 km, and 1.2 km, respectively. Velocity models shown in Fig. 16a–c represent realistic cases for seismic exploration studies where a very detailed velocity model is not always readily available. However, even in those cases, Fig. 17 shows that the Marchenko algorithm retrieves the Green's function with high accuracy.

When a smoothed velocity model is used for the Marchenko algorithm, the retrieved Green's function recovers the multiple reflections with some time shifts (Wapenaar et al., 2014a). Therefore, we also calculate time-shifted CCs (again excluding the direct wave) for a better evaluation of the retrieved Green's functions' accuracy using the Marchenko method. We apply a range of time shifts to the retrieved Green's functions using the smoothed velocity models shown in Fig. 16 and select the highest CC for a given time shift. Figure 18 shows the CCs after

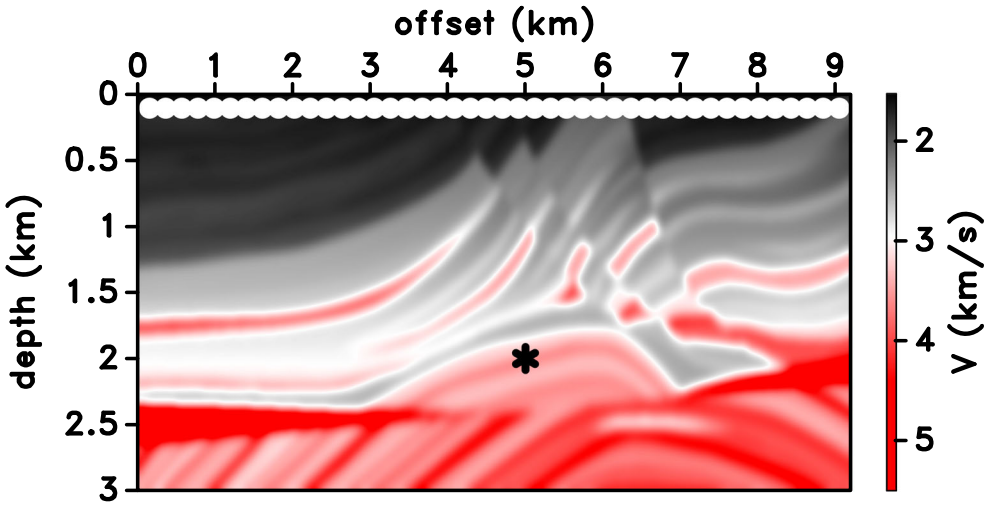

Figure 23
Less smoothed version of the Marmousi velocity model used for the iterative algorithm. The black asterisk shows the virtual source location and the white dots at the top indicate every 30th source/receiver location

applying a time shift of 0.8 ms, 1.2 ms, 2.4 ms, 4.8 ms, 9.6 ms, and 25.6 ms to the retrieved Green's functions using the smoothing radius of 0.05 km, 0.25 km, 0.45 km, 0.65 km, 0.85 km, and 1.2 km, respectively. Figure 18 shows that the CCs between the time-shifted Green's function and the modeled Green's function improve dramatically in comparison with the zero-shift CCs of Fig. 17. Whereas the average CC for the smoothing radius of 1.2 km in Fig. 17 is −0.11, we observe an average CC of 0.6 in Fig. 18 after applying a 25.6 ms time shift to the retrieved Green's function. This example clearly shows the benefit of evaluating time-shifted CCs.

5. *Refracted Waves*

In this section, we investigate the presence of refracted waves in the retrieved Green's function using the Marchenko focusing. To model refracted waves in the Green's functions, we use the Marmousi velocity model (Versteeg, 1994) for the numerical experiments in this section. Figure 19a shows the Marmousi velocity model and Fig. 19b shows the density model of our experiment. The white dots in Fig. 19 represent every 30th receiver location at the surface and the black asterisk denotes the virtual source location for which the Green's function will be retrieved. Figure 20 shows the modeled reflection data using the velocity and density models shown in Fig. 19a and b, respectively, with the receivers and source located at the surface where the refracted waves are present between receiver number 800 and 1320.

To start the iterative algorithm, we model the direct wave using the smoothed background velocity model shown in Fig. 21, and the modeled direct wave is shown in Fig. 22a. The red arrows in Fig. 22a point to some of the triplicated arrivals and the blue arrow points out the refracted wave. After following the iterative scheme, we show the retrieved Green's function after four iterations in Fig. 22b, and the numerically modeled Green's function for the virtual source location in Fig. 22c. The red dashed curve in Fig. 22b indicates the arrival of the direct wave (including some triplicated waves), and the waves before the red dashed curve in Fig. 22b can be removed by applying a muting function. The main difference in Fig. 22 between the retrieved and the modeled Green's functions (Figs. 22b and c, respectively) occurs between the receivers 800 and 1320 around the arrival time of the direct wave (around the red dashed curve in Fig. 22b). The numerically modeled Green's function (Fig. 22c) contains

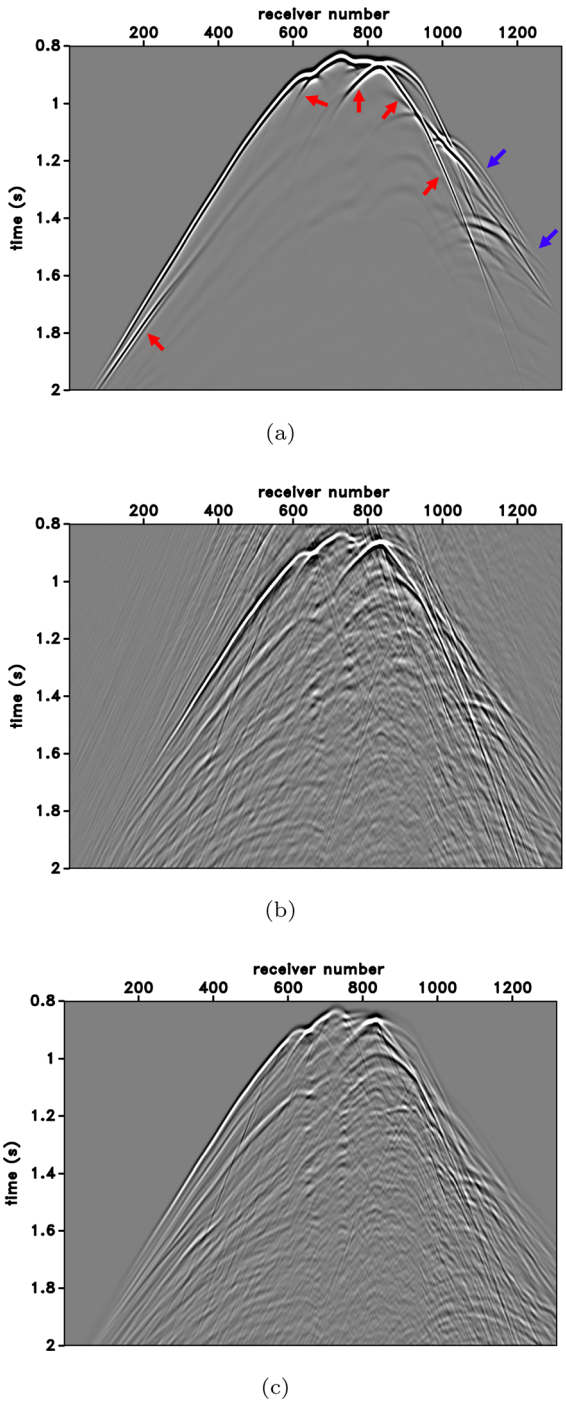

◀Figure 24
a Modeled direct wave using the less smoothed version of the Marmousi velocity model given in Fig. 23. The red arrows show some of the triplicated arrivals and the blue arrows show the refracted wave. **b** Retrieved Green's function using the Marchenko focusing using the less smoothed version of the Marmousi velocity model. **c** Numerically modeled Green's function (which is the same wavefield as Fig. 22c)

refracted and horizontally propagating events recorded between the receivers 800 and 1320 before the arrival time of the direct wave (also indicated with the red dashed curve in Fig. 22b). However, except for the refracted and horizontally propagating events shown in Fig. 22a, most of the refracted and horizontally propagating events in Fig. 22c are not present in the retrieved Green's function shown in Fig. 22b.

To further investigate the presence of the refracted wave in the Marchenko focusing, we use a less smoothed version of the Marmousi velocity model than the one shown in Fig. 21 which presents more detailed subsurface information. Figure 23 shows the less smoothed Marmousi model and the white dots show every 30th receiver location and the black asterisk denotes the virtual source location. The modeled direct wave using the less smoothed Marmousi model is shown in Fig. 24a, and the red arrows indicate some of the triplicated arrivals, and the blue arrows indicate the refracted wave. There are also some multiples modeled in Fig. 24a. Figure 24b shows the retrieved Green's function by using the direct wave in Fig. 24a, and c shows the numerically modeled Green's function. This time, between the receivers 800 and 1320 and around the direct arrival times, the retrieved Green's function and the numerically modeled Green's function match very well. The refracted wave information in the modeled Green's function is also present in the retrieved Green's function. The less smoothed version of the background velocity model used for the iterative algorithm enables the refracted waves to appear in the retrieved Green's function.

If we compare the modeled direct waves in Fig. 22a and 24a, the direct wave modeled with an accurate velocity model in Fig. 24a includes the refracted waves, shown with the blue arrows, but the modeled direct wave in Fig. 22a does not include most of these refracted waves. Figures 22b and 24b show that the refracted waves modeled using the smooth velocity model are mapped directly in the

retrieved Green's functions. In other words, the presence of refracted waves depends on the background velocity model in the Marchenko focusing and it is not a result of the iterations of the Marchenko focusing algorithm.

To further investigate the refracted wave presence in the retrieved Green's function using the Marchenko algorithm, we apply different degrees of smoothing to the Marmousi velocity model shown in Fig. 19a and model the direct waves using the smoothed velocity models. We then calculate the trace-by-trace CCs between the true direct wave

Figure 26
Modeled direct waves using the velocity models in Fig. 25a–f shown in **a**, **b**, **c**, **d**, **e**, and **f**, respectively ▶

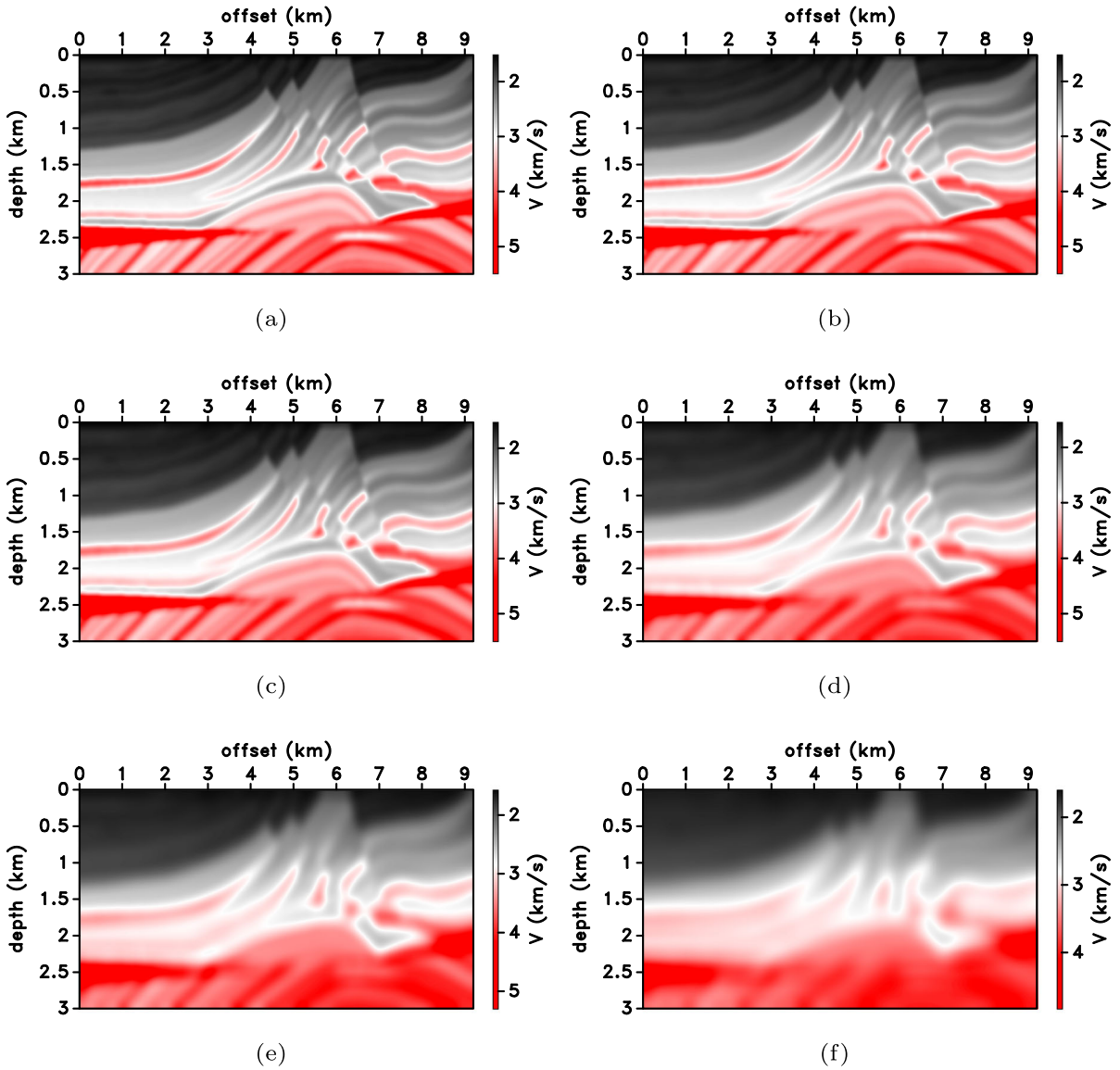

Figure 25
Marmousi velocity model in Fig. 19a after applying smoothing with a radius of 0.08 km, 0.09 km, 0.11 km, 0.16 km, 0.2 km, and 0.3 km, shown in **a**, **b**, **c**, **d**, **e**, and **f**, respectively

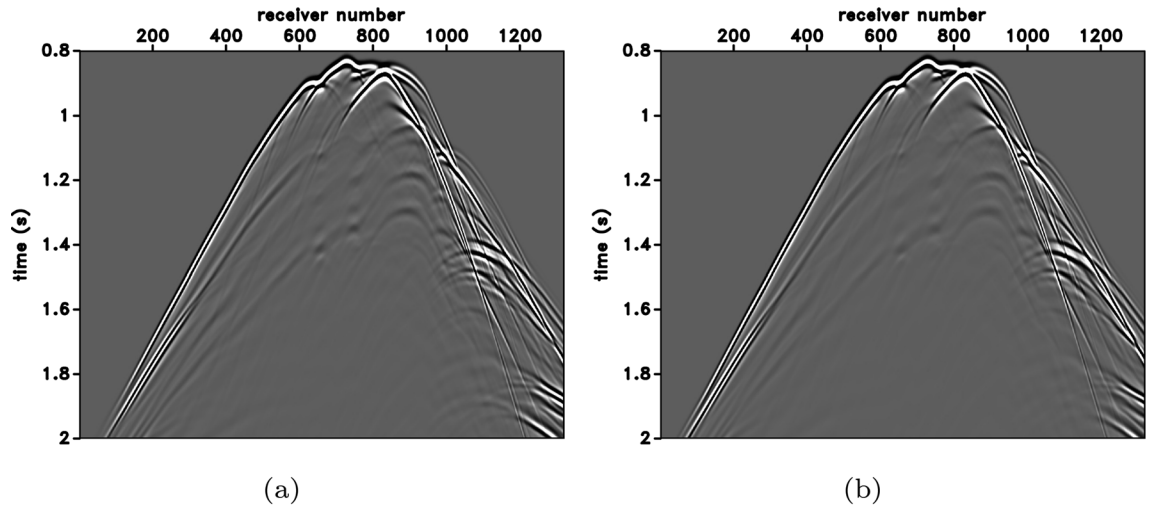
receiver number
200
400
600
800
1000
1200
time (s)
0.8
1
1.2
1.4
1.6
1.8
2

(a) (b)

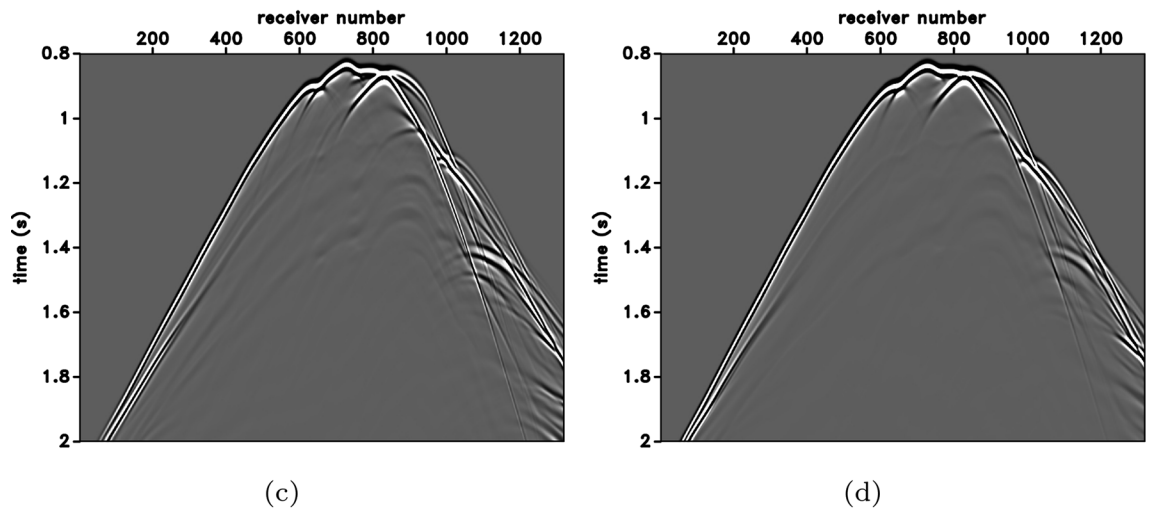
receiver number
200
400
600
800
1000
1200
time (s)
0.8
1
1.2
1.4
1.6
1.8
2

(c) (d)

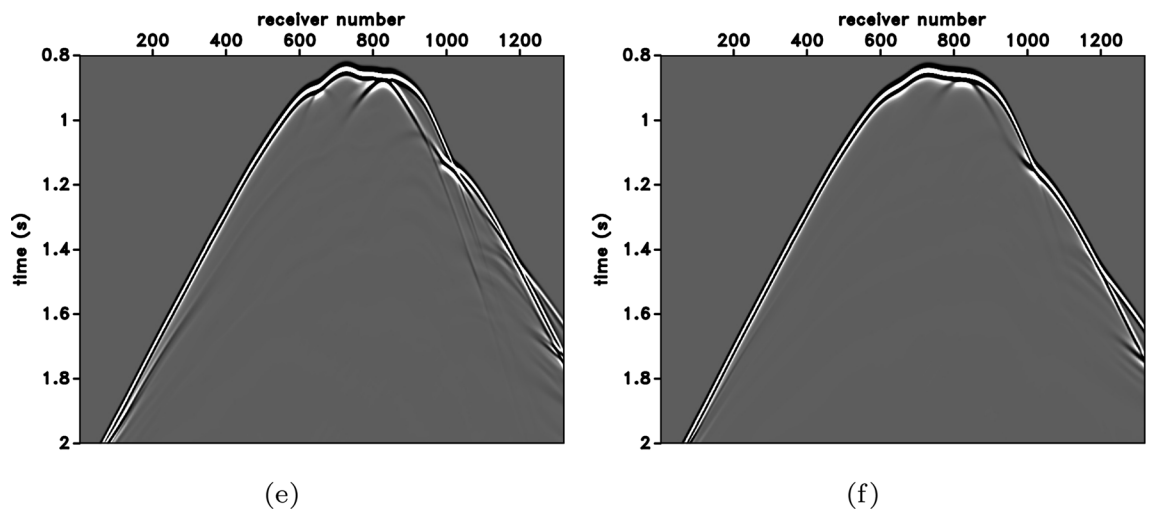
receiver number
200
400
600
800
1000
1200
time (s)
0.8
1
1.2
1.4
1.6
1.8
2

(e) (f)

(which is obtained using a smoothing radius of 0.032 km that includes the triplicated waves, refracted waves, and some reflected waves) and the modeled direct waves. Figure 25a–f show Marmousi velocity models with a smoothing radius of 0.08 km, 0.09 km, 0.11 km, 0.16 km, 0.2 km, and 0.3 km, respectively, applied on offset and depth (or x and z, respectively) axes using the triangle smoothing filtering in the Madagascar software package (Fomel et al., 2013; Claerbout, 2014). Figure 26a–f show the modeled direct waves using the velocity models shown in Fig. 25a–f, respectively. Figure 27 shows the CCs between the true and modeled direct waves shown in Fig. 26. The blue, orange, green, red, purple, and brown lines in Fig. 27 denote the CCs between the true and modeled direct waves using the smoothing radius of 0.08 km, 0.09 km, 0.11 km, 0.16 km, 0.2 km, and 0.3 km, respectively. Figure 27 shows for this example that for a triplicated and refracted wave presence with an average CC of 0.8 and higher in the direct wave, and hence in the retrieved Green's function, one needs to have a detailed velocity model with a smoothing radius of around 0.09 km or less (e.g., Fig. 26a and b). Figure 28a–f show the retrieved Green's functions using the direct waves shown in Fig. 26a–f, respectively.

A comparison of the CCs in Figs. 18 and 27 shows that considerably more accurate velocity model information is required for the presence of refracted waves in the retrieved Green's function (e.g., smoothing radius of 0.09km for an average CC of 0.8) than for accurately retrieving the reflected waves (e.g., smoothing radius of 0.65 km for an average CC of 0.8) using the Marchenko algorithm. Retrieving the refracted waves in the Green's function can be useful for velocity model building where the long-offset refracted and diving waves are of great importance for subsalt targets. In this case, the Marchenko algorithm we present requires a more accurate velocity model. Moreover, more research is needed to retrieve refracted and diving waves beyond those already present in the modeled direct wave. However, retrieving only the reflected waves is also very important for creating an accurate image of the subsurface using the conventional Marchenko imaging algorithms. In this case, the Marchenko algorithm requires a less accurate velocity model to be available and yet it retrieves the internal multiple reflections with high accuracy.

6. Conclusions

We present the Green's function retrieval using Marchenko focusing and investigate the background velocity model dependence of the Marchenko focusing. We compare the retrieved Green's functions for different background velocity models used for modeling the direct wave. We show that the Marchenko focusing algorithm using a constant background velocity model can retrieve the Green's function with high accuracy if the average slowness

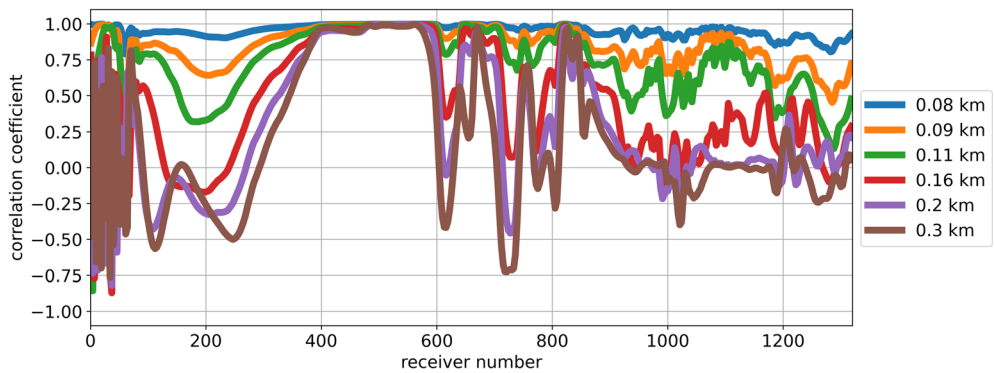

Figure 27
CCs between the true and modeled direct waves using the smoothing radius of 0.08 km, 0.09 km, 0.11 km, 0.16 km, 0.2 km, and 0.3 km, denoted with the blue, orange, green, red, purple, and brown lines, respectively

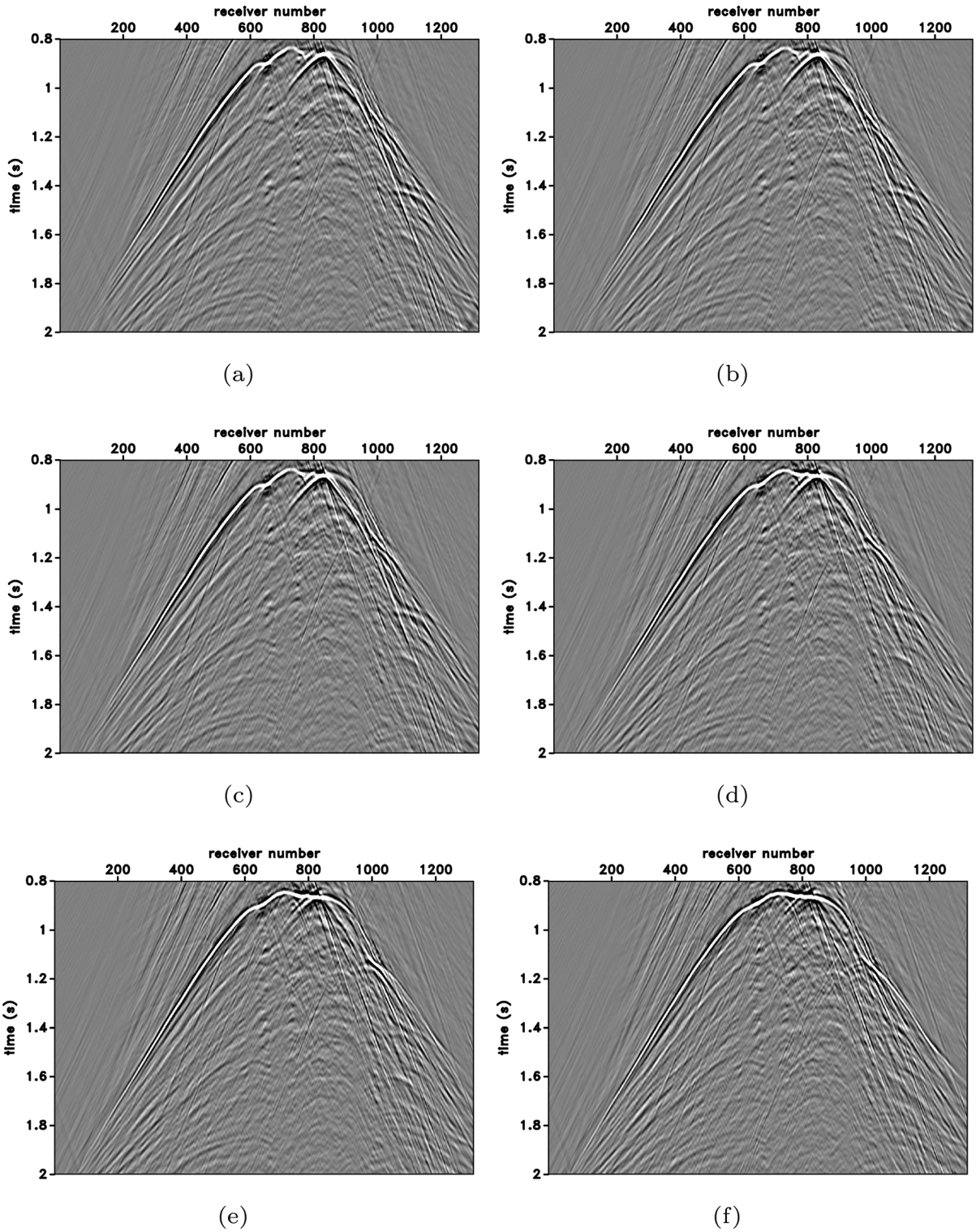

Figure 28
Retrieved Green's functions using the direct waves shown in Fig. 26a–f shown in **a**, **b**, **c**, **d**, **e**, and **f**, respectively

between the surface and the depth of the focal point is known. We also investigate the presence of the refracted waves in the retrieved Green's function using the Marmousi velocity model. We show that the refracted waves are incorporated in the retrieved Green's function by the background velocity model used to model the direct wave for the iterative algorithm, and are not a result of the Marchenko algorithm. The results from the refracted wave study indicate that substantially more accurate knowledge of the velocity model is required in the presence of refracted waves.

Author Contributions M.S.R.K. wrote the paper and conducted the numerical examples. R.S. advised M.S.R.K. during the manuscript preparation. K.W. gave constructive feedback and suggested further improvements.

Funding

This work is supported by the Consortium Project on Seismic Inverse Methods for Complex Structures at the Colorado School of Mines. The numerical examples in this paper were generated using the Madagascar software package (Fomel et al., 2013). The research of K. Wapenaar has received funding from the European Research Council (grant no. 742703).

Data Availability

No datasets were generated or analysed during the current study.

Declarations

Conflict of interest The authors declare no Conflict of interest.

Publisher's Note Springer Nature remains neutral with regard to jurisdictional claims in published maps and institutional affiliations.

References

Agranovich, Z., & Marchenko, V. (1963). *The inverse problem of scattering theory*. Gordon and Breach.

Behura, J., Wapenaar, K., & Snieder, R. (2014). Autofocus imaging: Image reconstruction based on inverse scattering theory. *Geophysics, 79*(3), A19–A26. https://doi.org/10.1190/geo2013-0398.1

Broggini, F., & Snieder, R. (2012). Connection of scattering principles: A visual and mathematical tour. *European Journal of Physics, 33*(3), 593–613.

Burridge, R. (1980). The Gelfand-Levitan, the Marchenko and the Gopinath-Sondhi integral equations of inverse scattering theory, regarded in the context of inverse impulse-response problems. *Wave Motion, 2*(4), 305–323.

Chadan, K., & Sabatier, P. C. (1989). *Inverse problems in quantum scattering theory*. Springer.

Claerbout, J. (2014). *Geophysical image estimation by example*. Stanford University.

Colton, D., & Kress, R. (1998). *Inverse acoustic and electromagnetic scattering theory*. Springer.

da Costa Filho, C. A., Ravasi, M., Andrew, C., & Meles, G. A. (2014). Elastodynamic Green's function retrieval through single-sided Marchenko inverse scattering. *Physical Review E, 90*, Article 063201. https://doi.org/10.1103/PhysRevE.90.063201

da Costa Filho, C. A., Ravasi, M., & Curtis, A. (2015). Elastic P- and S-wave autofocus imaging with primaries and internal multiples. *Geophysics, 80*(5), S187–S202. https://doi.org/10.1190/geo2014-0512.1

Derode, A., Larose, E., Campillo, M., & Fink, M. (2003). How to estimate the Green's function for a heterogeneous medium between two passive sensors? Application to acoustic waves. *Applied Physics Letters, 83*, 3054–3056.

Diekmann, L., & Vasconcelos, I. (2021). Focusing and Green's function retrieval in three-dimensional inverse scattering revisited: A single-sided Marchenko integral for the full wave field. *Physical Review Research, 3*, Article 013206.

Fomel, S., Sava, P., Vlad, I., Liu, Y., & Bashkardin, V. (2013). Madagascar: Open-source software project for multidimensional data analysis and reproducible computational experiments. *Journal of Open Research Software, 1*(1), Article e8.

Gel'fand, I., & Levitan, B. (1955). On the determination of the differential equation from its spectral function. *American Mathematical Society Translations, 2*(1), 253–304.

Gladwell, G. M. L. (1993). *Inverse problems in scattering*. Kluwer Academic Publishing.

Jia, X., Baumstein, A., Jing, C., Neumann, E., & Snieder, R. (2021). Subbasalt Marchenko imaging with offshore Brazil field data. *Geophysics, 86*, WC31–WC40. https://doi.org/10.1190/geo2020-0775.1

Jia, X., Guitton, A., & Snieder, R. (2018). A practical implementation of subsalt Marchenko imaging with a gulf of Mexico data set. *Geophysics, 83*(5), S409–S419.

Kiraz, M.S.R., & Snieder, R. (2022). Marchenko focusing using convolutional neural networks. *Second International Meeting for Applied Geoscience & Energy*, 1930-1934

Kiraz, M. S. R., & Nowack, R. L. (2018). Marchenko redatuming and imaging with application to the Frio carbon sequestration experiment. *Geophysical Journal International, 215*(3), 1633–1643.

Kiraz, M. S. R., Snieder, R., & Wapenaar, K. (2020). Marchenko focusing without up/down decomposition. *SEG Technical Program Expanded Abstracts, 2020*, 3593–3597.

Kiraz, M. S. R., Snieder, R., & Wapenaar, K. (2021). Focusing waves in an unknown medium without wavefield decomposition. *JASA Express Letters, 1*(5), Article 055602. https://doi.org/10.1121/10.0004962

Lomas, A., & Curtis, A. (2019). An introduction to Marchenko methods for imaging. *Geophysics, 84*(2), F35–F45. https://doi.org/10.1190/geo2018-0068.1

Marchenko, V. (1955). The construction of the potential energy from the phases of scattered waves. *Doklady Akademii Nauk, 104*, 695–698.

Meles, G. A., Löer, K., Ravasi, M., Curtis, A., & da Costa Filho, C. A. (2015). Internal multiple prediction and removal using Marchenko autofocusing and seismic interferometry. *Geophysics, 80*(1), A7–A11. https://doi.org/10.1190/geo2014-0408.1

Meles, G. A., Wapenaar, K., & Curtis, A. (2016). Reconstructing the primary reflections in seismic data by Marchenko redatuming and convolutional interferometry. *Geophysics, 81*(2), Q15–Q26. https://doi.org/10.1190/geo2015-0377.1

Newton, R. G. (1980). Inverse scattering. I. one dimension. *Journal of Mathematical Physics, 21*(3), 493–505.

Oristaglio, M. L. (1989). An inverse scattering formula that uses all the data. *Inverse Problems, 5*(6), 1097–1105.

Paffenholz, J., Stefani, J., McLain, B., Bishop, K. (2002). Sigsbee_2a synthetic subsalt dataset - image quality as function of migration algorithm and velocity model error. *Presented at the 64th EAGE Conference & Exhibition, European Association of Geoscientists & Engineers*, https://doi.org/10.3997/2214-4609-pdb.5.B019

Ravasi, M., Vasconcelos, I., Kritski, A., Andrew, C., da Costa Filho, C. A., & Meles, G. A. (2016). Target-oriented Marchenko imaging of a North Sea field. *Geophysical Journal International, 205*(1), 99–104.

Reinicke, C., Dukalski, M., & Wapenaar, K. (2020). Comparison of monotonicity challenges encountered by the inverse scattering series and the marchenko demultiple method for elastic waves. *Geophysics, 85*(5), Q11–Q26.

Rodgers, J. L., & Nicewander, W. A. (1988). Thirteen ways to look at the correlation coefficient. *American Statistician, 42*(1), 59–66.

Rose, J. H. (2002). Time reversal, focusing and exact inverse scattering. In M. Fink, W. A. Kuperman, J. P. Montagner, & A. Tourin (Eds.), *Imaging of complex media with acoustic and seismic waves, Topics in Applied Physics.* (Vol. 84). Berlin, Heidelberg: Springer.

Rose, J. H. (2001). "Single-sided'' focusing of the time-dependent Schrödinger equation. *Physical Review A, 65*(1), Article 012707.

Snieder, R., & Larose, E. (2013). Extracting Earth's elastic wave response from noise measurements. *Ann. Rev. Earth Planet. Sci.,41*, 183–206. http://arjournals.annualreviews.org/eprint/Yba7vHbEPazD9Ryqy38M/full/10.1146/annurev-earth-050212-123936

Staring, M., Dukalski, M., Belonosov, M., Baardman, R. H., Yoo, J., Hegge, R. F., & Wapenaar, K. (2021). Robust estimation of primaries by sparse inversion and Marchenko equation-based workflow for multiple suppression in the case of a shallow water layer and a complex overburden: A 2D case study in the Arabian Gulf. *Geophysics, 86*(2), Q15–Q25.

Thorbecke, J., Slob, E., Brackenhoff, J., van der Neut, J., & Wapenaar, K. (2017). Implementation of the Marchenko method. *Geophysics, 82*(6), WB29–WB45. https://doi.org/10.1190/geo2017-0108.1

Thorbecke, J., Zhang, L., Wapenaar, K., & Slob, E. (2021). Implementation of the Marchenko multiple elimination algorithm. *Geophysics, 86*(2), F9–F23. https://doi.org/10.1190/geo2020-0196.1

van der Neut, J., Wapenaar, K., Thorbecke, J., Slob, E., & Vasconcelos, I. (2015). An illustration of adaptive Marchenko imaging. *The Leading Edge, 34*(7), 818–822.

Versteeg, R. (1994). The Marmousi experience: Velocity model determination on a synthetic complex data set. *The Leading Edge, 13*(9), 927–936.

Wapenaar, K. (2014). Single-sided Marchenko focusing of compressional and shear waves. *Physical Review E, 90*, Article 063202. https://doi.org/10.1103/PhysRevE.90.063202

Wapenaar, K., Broggini, F., Slob, E., & Snieder, R. (2013). Three-dimensional single-sided Marchenko inverse scattering, data-driven focusing, Green's function retrieval and their mutual relations. *Physical Review Letters, 110*, Article 084301.

Wapenaar, K., Fokkema, J., & Snieder, R. (2005). Retrieving the Green's function in an open system by cross correlation: A comparison of approaches (L). *The Journal of the Acoustical Society of America, 118*(5), 2783–2786.

Wapenaar, K., Snieder, R., de Ridder, S., & Slob, E. (2021). Green's function representations for Marchenko imaging without up/down decomposition. *Geophysical Journal International, 227*(1), 184–203.

Wapenaar, K., Thorbecke, J., van der Neut, J., Broggini, F., Slob, E., & Snieder, R. (2014). Green's function retrieval from reflection data, in absence of a receiver at the virtual source position. *Journal of the Acoustical Society of America, 135*(5), 2847–2861.

Wapenaar, K., Thorbecke, J., van der Neut, J., Broggini, F., Slob, E., & Snieder, R. (2014). Marchenko imaging. *Geophysics, 79*(3), WA39–WA57.

Weaver, R., & Lobkis, O. (2001). Ultrasonics without a source: Thermal fluctuation correlations at MHz frequencies. *Physical Review Letters, 87*(13), Article 134301.

(Received January 9, 2024, revised October 12, 2025, accepted November 15, 2025, Published online November 28, 2025)